

1       **From salinity to nanoplastics: redefining safe yield in strip-island**

2                   **aquifers under emerging contaminant threats**

3                   **Tianyuan Zheng<sup>1,2,3\*</sup>, Chunxiang Ma<sup>1,2,3</sup>, Shaobo Gao<sup>1,2,3\*\*</sup>, Jian Luo<sup>4</sup>**

4       <sup>1</sup> College of Environmental Science and Engineering, Ocean University of China,

5       Qingdao, China, Qingdao 266100, China.

6       <sup>2</sup> Key Laboratory of Marine Environment and Ecology, Ministry of Education, Ocean

7       University of China, Qingdao 266100, China.

8       <sup>3</sup> Shandong Provincial Key Laboratory of Marine Engineering Geology and the

9       Environment, Ocean University of China, Qingdao 266100, China.

10      <sup>4</sup> School of Civil and Environmental Engineering, Georgia Institute of Technology,

11      Atlanta, GA 30332, USA.

12      Corresponding authors: Tianyuan Zheng ([zhengtianyuan@ouc.edu.cn](mailto:zhengtianyuan@ouc.edu.cn));

13                   Shaobo Gao ([gaoshaobo@ouc.edu.cn](mailto:gaoshaobo@ouc.edu.cn))

14

15 **Abstract:** Nanoplastic contamination is emerging as a significant threat to  
16 groundwater security on small islands, where freshwater lenses serve as primary  
17 water supplies. Existing groundwater management frameworks are largely based on  
18 salinity intrusion and do not account for the distinct transport behavior of nanoplastics.  
19 This study formulates a multi-physics numerical model incorporating variable-density  
20 groundwater flow, salt transport, and nanoplastic migration processes to investigate  
21 nanoplastic transport in idealized strip-island aquifers under pumping conditions. The  
22 model is calibrated using laboratory-scale data and evaluated at the field scale.  
23 Results show that nanoplastic migration is controlled not only by advection –  
24 dispersion processes but also by particle-specific interactions, leading to transport  
25 dynamics fundamentally different from those of dissolved salts. In particular, the  
26 higher effective dispersivity of nanoplastics causes earlier breakthrough at extraction  
27 wells and the formation of broader contaminant transition zones. Pronounced scale  
28 effects are observed: while laboratory simulations exhibit rapid upward coning and  
29 contamination, field-scale simulations indicate attenuated coning and stabilization  
30 over substantially longer timeframes. Sensitivity analysis identifies nanoplastic  
31 dispersivity as the dominant parameter influencing well contamination risk. These  
32 findings demonstrate that safe extraction strategies based solely on salinity thresholds  
33 may underestimate contamination risks and that well placement and pumping design  
34 must account for nanoplastic transition zones. The study provides a process-based  
35 framework for adapting groundwater management to emerging nanoplastic pollution  
36 in vulnerable island environments.

37 **Keywords:** Groundwater lens; Seawater intrusion; Groundwater contamination;

38 Pumping optimization

39

40 **1. Introduction**

41 Islands, ~~more than 340,000 worldwide,~~ host nearly 10% of the global  
42 population and cover approximately 6.7% of the ~~Earth's~~Earth's terrestrial surface ~~and~~  
43 ~~support nearly 10% of the global population~~ (Sayre et al., 2019). On many small  
44 islands, limited surface water availability makes groundwater a critical resource for  
45 local communities (Dose et al., 2014). Notably, numerous Pacific islands rely on  
46 shallow freshwater lenses—buoyant bodies of freshwater overlying saltwater in  
47 highly permeable aquifers—as their primary water supply (Sharan et al., 2021; White  
48 and Falkland, 2010). The formation, stability, and morphology of these lenses result  
49 from the interplay between density contrasts and multiple external factors, including  
50 climate, geological structures, and anthropogenic activities such as groundwater  
51 pumping and subsurface barrier installation (Alsumaiei and Bailey, 2018; Ketabchi et  
52 al., 2014; Tang et al., 2021, 2022; Yan et al., 2021; Yang et al., 2025; Gao et al., 2025;  
53 Zheng et al., 2025). ~~A persistent challenge is the sustainable extraction of freshwater,~~  
54 ~~as excessive~~Excessive pumping ~~can induce upward~~readily induces saline ~~coning,~~  
55 ~~degrade~~upconing, degrades water quality, and ~~threaten~~threatens long-term water  
56 security (Abdoulhalik and Ahmed, 2018; Dagan and Bear, 1968; Houben and Post,  
57 2017; Werner et al., 2009).

58 ~~The maximum safe extraction rate for freshwater lenses is typically estimated~~  
59 ~~using analytical solutions that assume a sharp interface between freshwater and~~  
60 ~~seawater (Muskat, 1937). Such approaches are widely used in two-dimensional~~  
61 ~~strip-island models to determine the pumping threshold at which the saline interface~~  
62 ~~reaches the well screen (Tang et al., 2020, 2021, 2024). While computationally~~  
63 ~~efficient, these models neglect hydrodynamic dispersion and the development of a~~  
64 ~~brackish transition zone, which can be extensive in highly permeable island aquifers~~  
65 ~~(Coulon et al., 2022; Babu et al., 2020). Consequently, current safe yield assessments~~  
66 ~~often overlook realistic mixing processes and contaminant transport within the~~  
67 ~~transition zone, potentially underestimating water quality risks.~~

68 Beyond salinity intrusion, microplasticnanoplastic contamination has emerged as

69 an additional and largely unaddressed threat to island groundwater systems.  
70 Microplastics are pervasive environmental pollutants detected in marine environments,  
71 soils, and groundwater worldwide (Koelmans et al., 2022; Koutnik et al., 2021; Li et  
72 al., 2018; Ren et al., 2021; Thompson et al., 2024). Oceanic concentrations continue  
73 to rise due to plastic persistence and ongoing inputs (Isobe et al., 2019). ~~The~~  
74 ~~concentrations of nanoplastics—which are formed as a result of their breakdown—are~~  
75 ~~even higher~~Nanoplastics, which are generated through the fragmentation of larger  
76 plastic debris and microplastics, may occur at even higher particle-number  
77 concentrations, with coastal waters often exhibiting higher levels than open-ocean  
78 regions (ten Hietbrink et al., 2025). Emerging evidence indicates that seawater  
79 intrusion facilitates the transport of microplastics into coastal aquifer systems (Chen  
80 et al., ~~2024~~2024a). Because island aquifers are completely surrounded by seawater,  
81 freshwater lenses are particularly vulnerable to marine-sourced nanoplastic  
82 contamination (Fig. 1).

83 The maximum safe extraction rate for freshwater lenses is typically estimated  
84 using analytical solutions that assume a sharp interface between freshwater and  
85 seawater (Muskat, 1938). Such approaches are widely used in two-dimensional  
86 strip-island models to determine the pumping threshold at which the saline interface  
87 reaches the well screen (Tang et al., 2020, 2021, 2024). While computationally  
88 efficient, these models neglect hydrodynamic dispersion and the development of a  
89 brackish transition zone, which can be extensive in highly permeable island aquifers  
90 (Coulon et al., 2022; Babu et al., 2020). Consequently, current safe-yield assessments  
91 often overlook realistic mixing processes and contaminant transport within the  
92 transition zone, potentially underestimating water-quality risks.

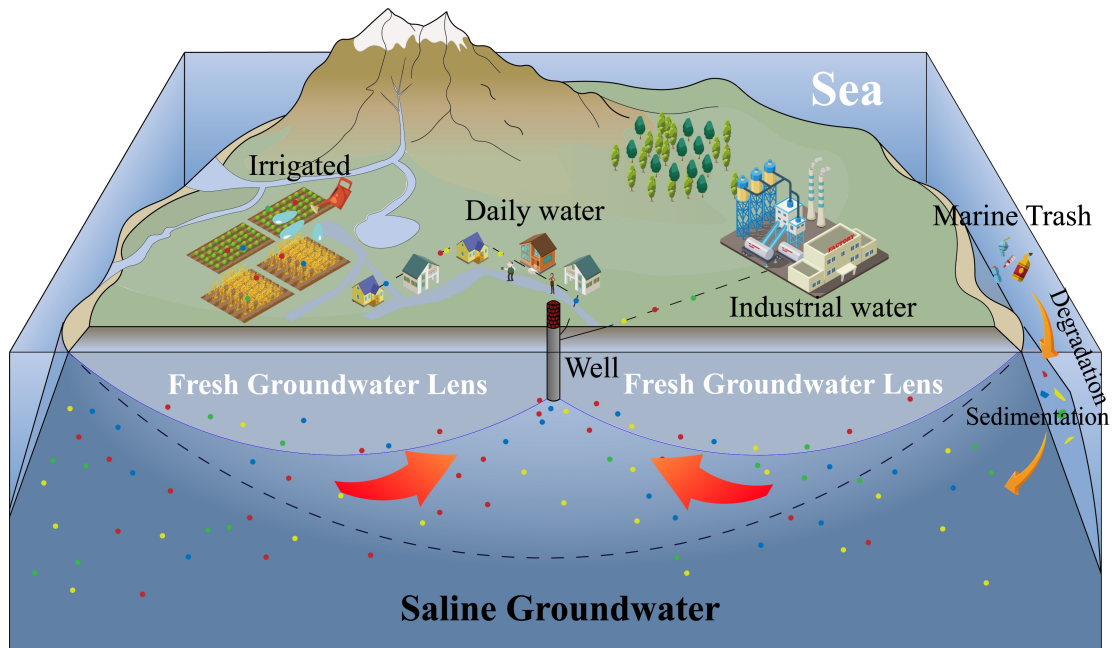
93 Transport processes of ~~microplastics~~nanoplastics in porous media differ  
94 fundamentally from those of dissolved solutes. Early modeling efforts adapted  
95 classical advection-dispersion equations with simple adsorption terms (Babakhani et  
96 al., 2017), but subsequent studies have demonstrated that the migration of  
97 microplastics and nanoplastics involves additional mechanisms such as

108 adsorption-desorption, clogging, interception, and aggregation (Liu et al., [2024](#)[2025](#);  
109 Yuan et al., 2024). Importantly, [microplastic](#) dispersion coefficients  
110 depend on particle size and flow velocity (Wang and Sedighi, 2023). Under pumping  
111 conditions that induce upward coning flow fields, these properties suggest that  
112 nanoplastics may migrate toward extraction wells more rapidly than [salinity-dissolved](#)  
113 [salts](#) and form a broader or earlier contaminant transition zone- ([Wang and Sedighi,](#)  
114 [2023](#); [Alkindi et al., 2011](#); [Lee et al., 2017](#)). Traditional sharp-interface and  
115 salinity-based intrusion models fail to capture this behavior, which has remained  
116 largely unexplored in island freshwater lens studies.

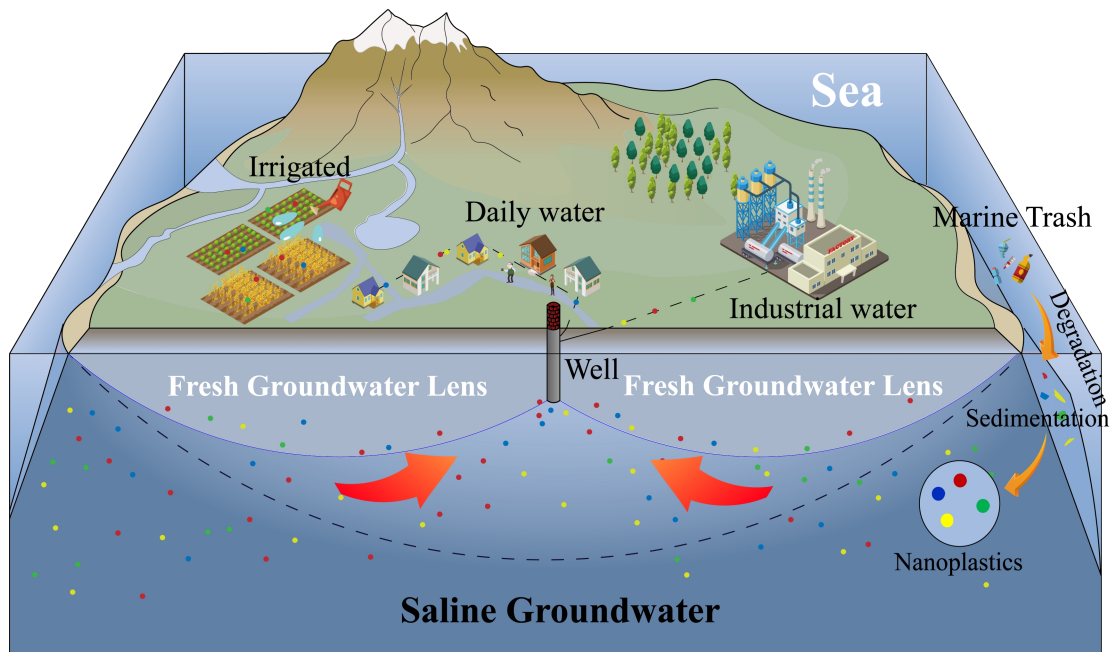
117 Taken together, there are two critical gaps- [that are interdependent and](#)  
118 [collectively undermine reliable groundwater management](#). First, existing safe-yield  
119 models oversimplify the freshwater-seawater transition zone by neglecting  
120 dispersion-driven mixing. [This oversimplification is further exacerbated when](#)  
121 [combined with the poorly characterized transport of nanoplastics, which exhibit](#)  
122 [unique migration dynamics that cannot be captured by traditional solute models](#).  
123 Second, the distinct migration behavior of nanoplastics under pumping-induced  
124 coning remains poorly understood. Current modeling frameworks, largely derived  
125 from solute transport theory, do not adequately capture transient nanoplastic  
126 breakthrough or particle-specific transport dynamics.

117 To address these gaps, this study develops a coupled numerical model that  
118 integrates variable-density groundwater flow, salt transport, and nanoplastic migration  
119 in island aquifers. This study aims to: (1) quantify marine-derived nanoplastic  
120 accumulation in freshwater extraction wells under pumping conditions; (2) assess how  
121 nanoplastic transport, especially enhanced dispersivity, alters the maximum safe  
122 extraction rate compared to traditional salinity-based thresholds; and (3) evaluate the  
123 sensitivity of nanoplastic migration and associated risks to key hydrogeological  
124 parameters and operational factors. By incorporating nanoplastic transport parameters  
125 derived from laboratory column experiments and conducting simulations at both  
126 laboratory and field scales, this work provides critical insights for adjusting

127 groundwater management strategies to safeguard island freshwater ~~resources~~resources  
128 in the face of emerging nanoplastic pollution.



129



130

131 Fig. 1. Schematic diagram of freshwater lenses and nanoplastic contaminant  
132 distribution in an idealized strip-island aquifer under groundwater extraction.

## 133 2. Methods

### 134 2.1 Mathematical model

135 To simplify the problem and enhance computational tractability, the following

136 key assumptions are adopted based on established modeling practices in coastal  
137 aquifer studies (Stoeckl and Houben, 2012; Yao et al., 2019): (i) the aquifer is  
138 homogeneous and isotropic; (ii) fluid density ~~is depends~~ solely ~~dependent~~—on  
139 groundwater salinity, with thermal effects considered negligible; (iii) the density of  
140 nanoplastic ~~partiele density particles~~ is assumed to be approximately equal to ~~thethat~~  
141 of water density (e.g., some, which is representative of neutrally buoyant or aged  
142 nanoplasties);nanoplastic particles; (iv) the saturated zone is initially saturated with  
143 seawater, and rainfall infiltration is spatially uniform and temporally constant; ~~and~~-(v)  
144 groundwater flow is simulated within a two-dimensional vertical profile of the strip  
145 island, leveraging the geometric symmetry of the idealized domain; and (vi) tidal  
146 influences are neglected, and constant head boundary conditions are imposed at the  
147 seawater interface.

148 This study presents an integrated numerical framework that extends a  
149 variable-density groundwater flow model for the unsaturated-saturated zone by  
150 incorporating salinity and ~~nanopartiele~~nanoplastic transport modules. The  
151 ~~nanopartiele~~nanoplastic transport model ~~uniquely~~——combines  
152 advective-~~diffusive~~ dispersive transport with nanoplastic adsorption mechanisms. The  
153 resulting framework simultaneously simulates variable-density groundwater flow,  
154 ~~soluted~~dissolved salt transport, and ~~nanopartiele~~nanoplastic migration via coupled  
155 advection-dispersion and adsorption processes. Governing equations for the  
156 variable-density flow and salinity transport components are available in Text S1.

157 Research suggests that nanoplastic transport is primarily influenced by particle  
158 movement and physical/physicochemical interactions with porous media surfaces (Al  
159 Harraq and Bharti, 2022; Ranjan et al., 2023; Ren et al., 2022; Waldschläger and  
160 Schüttrumpf, 2020). Particle movement is described in the equations as  
161 ~~convection~~advection, diffusion and dispersion effects, while physicochemical  
162 interactions with porous media are characterized by mechanisms such as adhesion and  
163 detachment, ~~mechanical~~ strainstraining on aggregates and individual particles,  
164 blockage, and maturation. The subsurface transport of nanoplastic particles is

165 governed by an advection-~~diffusion~~dispersion equation, a framework established for  
 166 nanopartielenanoplastic migration that captures advection, dispersion, and adsorption  
 167 processes (YuanLiu et al., 20242025):

$$\frac{\partial}{\partial t}(S_w \theta C_{np}) + \frac{\partial}{\partial t}(\rho_b s) + \nabla C_{np} \frac{k_r \mathbf{k}}{\mu} \nabla P + \nabla \cdot [-\theta S_w D_{np} \nabla C_{np}] = f \quad (1)$$

$$\frac{\rho_b \partial s}{\partial t} = \theta K_{att} \psi_b C_{np} e^{-\frac{s}{\lambda}} - \rho_b K_{det} s + \theta \rho_b K_{rip} s C_{np} \quad (2)$$

168 where  $C_{np}$  represents the concentration of nanoplastics in groundwater [ $ML^{-3}$ ],  $\rho_b$   
 169 denotes the bulk density of the aquifer medium [ $ML^{-3}$ ],  $s$  is the mass of  
 170 nanoplastics attached per unit mass of solid [ $MM^{-1}$ ],  $D_{np}$  is the hydrodynamic  
 171 dispersion coefficient of nanoplastics [ $L^2T^{-1}$ ], and  $f$  is the source-sink term  
 172 [ $ML^{-3}T^{-1}$ ].  $K_{att}$  is the first-order colloidal attachment coefficient [ $T^{-1}$ ], parameter  $\lambda$   
 173 represents the strain capacity of porous media [ $MM^{-1}$ ],  $K_{det}$  is the first-order colloidal  
 174 detachment coefficient [ $T^{-1}$ ], and  $K_{rip}$  is the agingripening kinetic rate coefficient  
 175 [ $M^{-1}L^3T^{-1}$ ].

176 The adhesion of nanoplastics in porous media is described by the following  
 177 governing equation:

$$\psi_b = \left(1 - \frac{s}{s_{max}}\right) \quad (3)$$

178 where  $\psi_b$  denotes the adhesion state of nanoplastics in porous media [-], and  $s_{max}$   
 179 represents the maximum mass of nanoplastics that can be retained per unit mass of  
 180 porous medium [ $MM^{-1}$ ].

181 The variation in hydraulic conductivity as a function of porosity is characterized  
 182 by the following relationship (Zheng, 2014):

$$\frac{K}{K_0} = \left(\frac{\theta}{\theta_0}\right)^3 \left(\frac{1-\theta_0}{1-\theta}\right)^3 \quad (4)$$

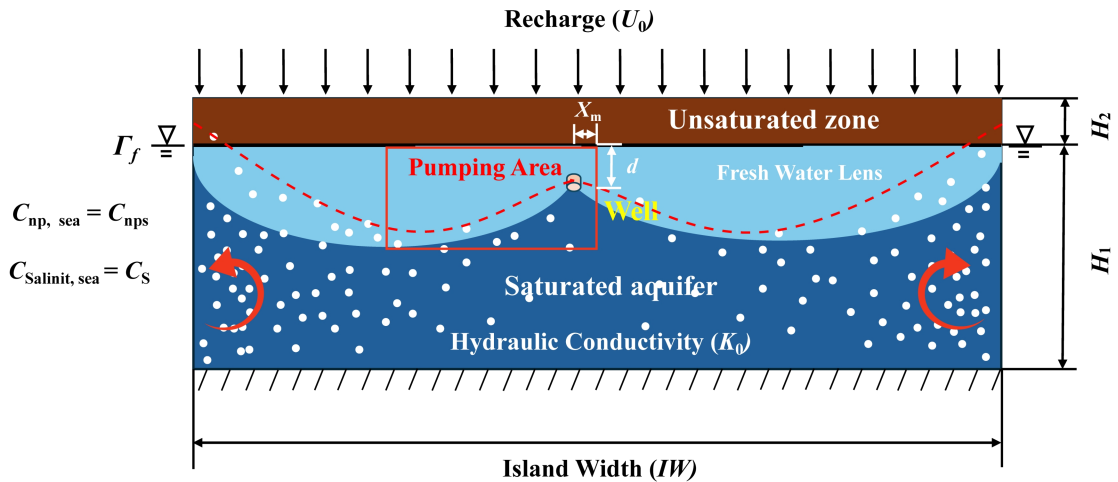
183 where  $K$  is the hydraulic conductivity of the porous medium [ $LT^{-1}$ ],  $K_0$  is the  
 184 hydraulic conductivity of the initial porous medium [ $LT^{-1}$ ], and  $\theta_0$  is the porosity of  
 185 the initial water-bearing medium [-].

186 The approximate analytical solution derived by Tang et al. (2021) describes the  
 187 critical pumping rate preventing brine intrusion when pumping wells are located in  
 188 the idealized strip island's central region. The theoretical maximum safe extraction  
 189 rate is expressed as:

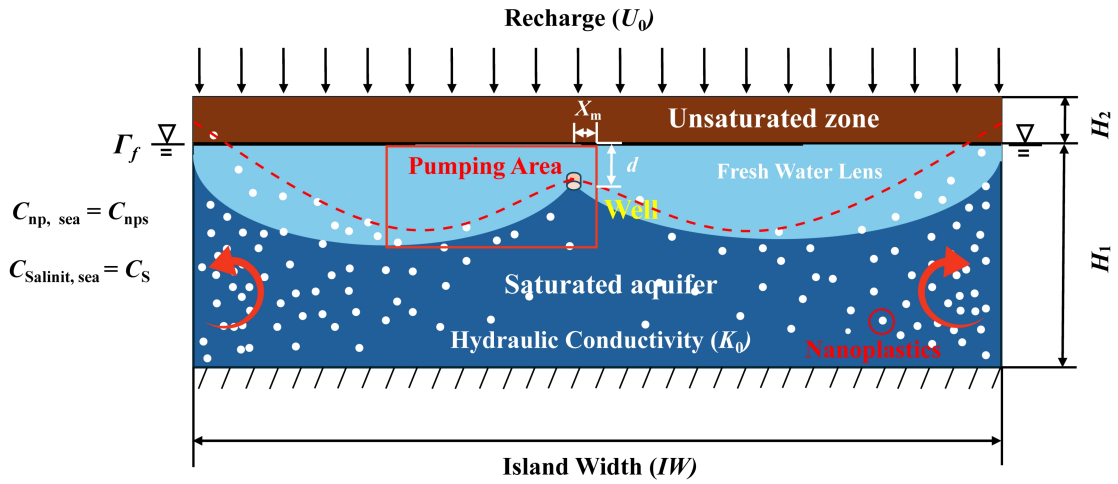
$$Q_{Tmax} = \omega(W - x_m) - \frac{\delta(1+\delta)Kd^2}{(W - x_m)} \quad (5)$$

$$\delta = \frac{(\rho_s - \rho_f)}{\rho_f} \quad (6)$$

190 where  $\omega$  is the infiltration rate at the upper surface of the unsaturated zone [ $LT^{-1}$ ],  
 191  $\rho_s$  is the ~~sea-water~~seawater density [ $ML^{-3}$ ],  $\rho_f$  is the ~~fresh-water~~freshwater density  
 192 [ $ML^{-3}$ ],  $d$  is the distance from the well to the lower boundary of the unsaturated zone  
 193 [ $L$ ],  $W$  is the half width of the idealized strip island [ $L$ ],  $x_m$  is the distance from the  
 194 well to the centre of the idealized strip island [ $L$ ].



195



196

197 Fig. 2. Conceptual model of nanoplastic pollution in an idealized strip-island aquifer  
 198 with central pumping. The model depicts an unsaturated zone (height  $H_2$ ) over a  
 199 saturated zone (height  $H_1$ ). Freshwater lenses are shown in light blue and saline  
 200 groundwater in dark blue. Key parameters include island width ( $IW$ ), continuous  
 201 precipitationrecharge ( $U_0$ ), seawater salinity ( $C_s$ ), and seawater nanoplastic  
 202 concentration ( $C_{nps}$ ).

## 203 2.2 Numerical SimulationSolution

204 The numerical simulation investigates the migration behavior of nanoplastics  
 205 under pumping conditions in an idealized strip-island aquifer. The laboratory-scale  
 206 model domain (60 cm×17 cm) was constructed following the configuration  
 207 established by Tang et al. (2021) (Fig. S4), while a field-scale model (600 m×50 m)  
 208 was developed to assess sitefield-level transport phenomena. Key simulation  
 209 parameters are provided in Table 1. Model parameters calibrated from  
 210 laboratory-scale experiments were extrapolated to the field scale assumed for the  
 211 modeling study to evaluate the consistency of nanoplastic migration patterns across  
 212 scales. At the ocean boundary, a constant head (Dirichlet) condition was imposed with  
 213 a specified hydraulic head ( $H_1$ ) and a salt concentration of 34.7 g/L; tidal influences  
 214 were neglected. A constant flux (Neumann) condition was applied to the upper  
 215 boundary, representing recharge at a rate  $U_0$ . Fig. 2 shows a vertical cross-section of a  
 216 typical freshwater groundwater lens in an idealized island under single-well pumping  
 217 conditions. Additional aquifer properties are summarized in Table 1.

218 **Table 1.** Numerical Simulation Parameters for Variable-Density Flow and Nanoplastic  
 219 Transport (Laboratory and Field Scales)

Parameter	Symbol	Unit	Value
<i>Variable density parameter</i>			
Density of sea water	$\rho_0$	kg/m <sup>3</sup>	1025
Density of freshwater	$\rho_f$	kg/m <sup>3</sup>	1000
<del>brine concentration</del> <u>Seawater salinity</u>	$C_s$	mol/L	0.5989
<i>Nanoplastics properties PS-Pd-1</i>			
<del>Constant a</del> <u>Constant<sup>a, b</sup></u>	$\lambda$	mg/gkg	1.6
<del>Particle deposition rate coefficient a,</del> <del>b</del> <u>First-order colloidal attachment</u> <u>coefficient<sup>a, b</sup></u>	$K_{att}$	1/s	0.0025
Euler <del>number a</del> <u>number<sup>a</sup></u>	$e$	—	2.7183
The maximum solid phase particle <del>concentration a</del> <u>concentration<sup>a, b</sup></u>	$S_{max}$	m <sup>3</sup> mg/kg	10
<del>Particle release rate coefficient a,</del> <del>b</del> <u>First-order colloidal detachment</u> <u>coefficient<sup>a, b</sup></u>	$K_{det}$	1/s	0.001
<del>Maturity Ripening kinetic</del> <del>rate of nanoplastics a</del> <u>coefficient<sup>a, b</sup></u>	$K_{rip}$	m <sup>3</sup> /(g·s·mol)	0.009
Longitudinal <del>dispersivity b</del> <u>dispersivity<sup>b</sup></u>	$\alpha_{LPS-Pd-1}$	cm	<u>0.914-0</u> <u>6</u>
The average relative molecular weight of <del>nanoplastics e</del> <u>nanoplastics<sup>c</sup></u>	$N_m$	g/mol	70000
<i>Nanoplastics properties PS-Pd-2</i>			
<del>Constant a</del> <u>Constant<sup>a, b</sup></u>	$\lambda$	mg/gkg	1.7
<del>Particle deposition rate coefficient a,</del>	$K_{att}$	1/s	0.0002

<u>First-order colloidal attachment coefficient<sup>a, b</sup></u>	<del>con</del>	$S_{max}$	$m^3mg/kg$	10
<u>Particle release rate coefficient a, b</u>		$K_{det}$	1/s	0.005
<u>First-order colloidal detachment coefficient<sup>a, b</sup></u>		$K_{rip}$	$m^3/(g \cdot s \cdot mol)$	0.007
<u>Maturity Ripening kinetic rate of nanoplastics a coefficient<sup>a, b</sup></u>		$\alpha_{LPS-Pd-2}$	cm	<del>1.060-9</del> ±
<u>Longitudinal dispersivity b dispersivity<sup>b</sup></u>		$N_m$	g/mol	70000
<u>nanoplastics nanoplastics<sup>c</sup></u>				
<b><i>Laboratory Porous medium properties</i></b>				
Island <del>width d</del> <u>width<sup>d</sup></u>		$IW$	cm	60
Saturated zone <del>thickness d</del> <u>thickness<sup>d</sup></u>		$H_1$	cm	15
Unsaturated zone <del>thickness d</del> <u>thickness<sup>d</sup></u>		$H_2$	cm	2
Rainfall <del>infiltration d</del> <u>infiltration<sup>d</sup></u>		$U_0$	cm/min	0.80
<del>Porosity d</del> <u>Porosity<sup>d</sup></u>		$\theta_0$	—	0.38
Longitudinal dispersivity		$\alpha_L$	cm	0.2
Hydraulic <del>conductivity d</del> <u>conductivity<sup>d</sup></u>		$K_0$	cm/min	200
<b><i>Field-scale Porous medium properties</i></b>				
Island width		$IW$	m	600
Saturated zone thickness		$H_1$	m	45
Unsaturated zone thickness		$H_2$	m	5
Rainfall infiltration		$U_0$	m/s	$2 \times 10^{-8}$
Porosity		$\theta_0$	—	0.38
Longitudinal dispersivity		$\alpha_L$	m	0.5

- 220 a. Data from Liu et al. ([2024](#)[2025](#))  
 221 b. Data inversion was performed based on the experimental [data](#).  
 222 c. Data from Singh et al. (2025)  
 223 d. Experimental water pumping scenario from Tang et al. (2021)

224 The coupled governing equations for variable-density saturated groundwater  
 225 flow and solute transport were solved numerically via COMSOL Multiphysics, with  
 226 boundary conditions prescribed accordingly. The system of equations was solved  
 227 iteratively using a preconditioned conjugate gradient (PCG) method with a relative  
 228 tolerance of  $1 \times 10^{-4}$ . Initial time steps of 0.001 s and 0.001 d were adopted for the  
 229 transient analyses.

230 The computational domain for the laboratory-scale model was discretized into  
 231 63,928 triangular elements and 32,350 nodes, with a maximum element diameter of 2  
 232 mm. For the field-scale model, the domain was discretized into 30,000 quadrilateral  
 233 elements and 30,651 nodes, with a maximum element diameter of 1 m. The selected  
 234 mesh sizes, in conjunction with the hydrodynamic dispersion parameters, conformed  
 235 to the Péclet number criterion to minimize numerical dispersion and ensure solution  
 236 stability (Voss and Provost, 2002):

$$Pe_1 = \frac{v_1 \Delta L_1}{D_1 + \alpha_{L1} v_1} \approx \frac{\Delta L_1}{\alpha_{L1}} = 1 \leq 4 \quad (7)$$

$$Pe_2 = \frac{v_2 \Delta L_2}{D_2 + \alpha_{L2} v_2} \approx \frac{\Delta L_2}{\alpha_{L2}} = 2 \leq 4 \quad (8)$$

237 where  $Pe_1$  is the Péclet number in laboratory-scale [-],  $Pe_2$  is the Péclet number in  
 238 [sitefield](#)-scale [-],  $\Delta L_1$  is the grid length in laboratory-scale [L],  $\Delta L_2$  is the grid  
 239 length in [sitefield](#)-scale [L],  $v_1$  is flow velocity in laboratory-scale [ $LT^{-1}$ ],  $v_2$  is flow  
 240 velocity in [sitefield](#)-scale [ $LT^{-1}$ ],  $D_1$  is diffusion coefficient in laboratory-scale

241  $[L^2T^{-1}]$ ,  $D_2$  is diffusion coefficient in sitefield-scale  $[L^2T^{-1}]$ ,  $\alpha_{L1}$  is the  
242 Longitudinal dispersivity in laboratory-scale  $[L]$ ,  $\alpha_{L2}$  is the  
243 Longitudinal dispersivity in sitefield-scale  $[L]$ .

244 Stabilization times for laboratory and field simulations were determined using a  
245 convergence criterion: the system was considered stable when the relative change in  
246 wellhead salinity and nanoplastic concentration was less than 1% over three  
247 consecutive time steps.

248 A continuous rainfall-driven model was developed to simulate freshwater lens  
249 dynamics and well extraction in an idealized island aquifer. The simulation comprises  
250 two distinct hydraulic phases: Phase I involves the formation of a stable freshwater  
251 lens under continuous rainfall infiltration and seawater intrusion; Phase II initiates  
252 groundwater extraction via a single pumping well, leading to the development of a  
253 stable saline upconing zone. In the laboratory-scale setup, the horizontal distance  $x_m$   
254 from the standardpumping well to the island center was set to 0, 2.5, 5, 7.5, 10, 12.5,  
255 15, 17.5, and 20 cm. The vertical distance  $d$  from the well screen to the base of the  
256 saturation zone was defined as 0, 5, 10, 12, 15, 18, 20, and 25 mm. Hydraulic  
257 conductivity  $K_0$  values were assigned as 150, 175, 200, 225, and 250 cm/min, with  
258 corresponding recharge rates  $U_0$  of 0.6, 0.7, 0.8, 0.9, and 1.0 cm/min. For the  
259 field-scale scenario, the pumping well was positioned at a horizontal distance  $x_m=5$  m  
260 from the island center, corresponding to a central well location. The hydraulic  
261 conductivity  $K_0$  was set to  $1 \times 10^{-4}$  m/s, with a recharge rate  $U_0 = 2 \times 10^{-8}$  m/s (Tang et  
262 al., 2021).

### 263 **2.3 Evaluation Indicators**

264 Nanoplastic concentrations at the wellhead were monitored to evaluate the  
265 impacts of nanoplastics on island freshwater lens development projects. The  
266 seawater-freshwater interface of the freshwater lens was designated as 0.347 g/L,  
267 corresponding to 1% seawater salinity. Contemporary laboratory investigations  
268 typically utilize nanoplastic concentrations ranging from 10  $\mu\text{g/L}$  to 100 mg/L. Owing

269 to constraints associated with nanoplastic preparation protocols and detection  
 270 capabilities, the migration parameters of nanoplastics in this study were derived under  
 271 an initial concentration of 10 mg/L. ~~To date, the highest measured nanoplastic~~  
 272 ~~concentrations in natural environments have reached 3.02 mg/L in the North Pacific,~~  
 273 ~~while a maximum concentration of 162 mg/L has been documented in relevant studies~~  
 274 ~~(Moore et al., 2001; Reddy et al., 2006). Sussarellu et al. (2016) reported that a~~  
 275 ~~nanoplastic concentration of 22 µg/L induced alterations in feeding behavior and~~  
 276 ~~reproductive disruption in oysters.~~ Nanoplastics at 100–500 µg/L can exert widespread  
 277 toxicity to marine organisms including bivalves, sea urchins, algae, and bacteria  
 278 (Gonçalves & Bebianno, 2021). Adopting the 1‰ seawater salinity threshold as a  
 279 reference for nanoplastic concentrations facilitates comparisons of migration patterns  
 280 between nanoplastics and dissolved salts under freshwater extraction scenarios in  
 281 idealized strip-shaped islands, while incorporating the biological toxicity of  
 282 nanoplastics as a critical constraint.

283 Concurrently, the distribution of nanoplastics within freshwater lenses is  
 284 characterized by comparing the volume reduction rate ( $VR$ ) of freshwater lenses over  
 285 a given time period:

$$VR = \frac{V_0 - V_w}{V_w} \quad VR = \frac{V_0 - V_w}{V_0} \quad (9)$$

286 where  $V_0 - V_w$  represents the volume of freshwater lenses ~~not yet pumped~~  
 287 ~~surrounded~~ by nanoplastics pollution [ $L^3$ ],  $V_w$  ~~represents~~  $V_0$  represents the volume of freshwater  
 288 lenses ~~after pumped~~ surrounded by saline water [ $L^3$ ].

289 Accounting for the implications of the transition zone theory for groundwater  
 290 pumping practices, the following indicator is defined: the ratio of the actual maximum  
 291 safe extraction capacity to the theoretical maximum safe extraction capacity ( $ASYR$ ):

$$ASYR = \frac{Q_{Amax}}{Q_{Tmax}} \quad (10)$$

292 where  $Q_{Amax}$  represents the actual maximum safe extraction volume [ $L^3T^{-1}$ ],  $Q_{Tmax}$   
 293 represents the theoretical maximum safe extraction volume [ $L^3T^{-1}$ ]

294 Taking into account the potential reduction in groundwater extraction capacity  
 295 induced by nanoplastic contamination, the following indicator is defined: the ratio of  
 296 the maximum safe extraction capacity reduction caused by nanoplastic retention to the  
 297 maximum safe extraction capacity (*RRSY*):

298

$$RRSY = \frac{Q_{Amax} - Q_{Smax}}{Q_{Amax}} \quad (11)$$

299 where  $Q_{Smax}$  represents the maximum safe extraction volume without nanoplastic  
 300 influence [ $L^3T^{-1}$ ].

301 Table 2 provides a systematic description of the representative roles of the three  
 302 evaluation metrics used in this paper:

303 **Table 2. Summary of Evaluation Indicators and Their Functions**

<u>Symbol</u>	<u>Full name</u>	<u>Description</u>
<u>VR</u>	<u>Volume reduction rate</u>	<u>Quantifies the shrinkage degree of usable freshwater lens volume under nanoplastic contamination.</u>
<u>ASYR</u>	<u>Ratio of the actual maximum safe extraction capacity to the theoretical maximum safe extraction capacity</u>	<u>Evaluates the reduction degree of practical safe extraction capacity relative to the theoretical threshold.</u>
<u>RRSY</u>	<u>Ratio of the maximum safe extraction capacity reduction caused by</u>	<u>Assesses the additional loss of safe extraction capacity specifically caused by nanoplastic retention and contamination.</u>

nanoplastic retention to the  
maximum safe extraction  
capacity

---

304

305 **2.4 Model Calibration**

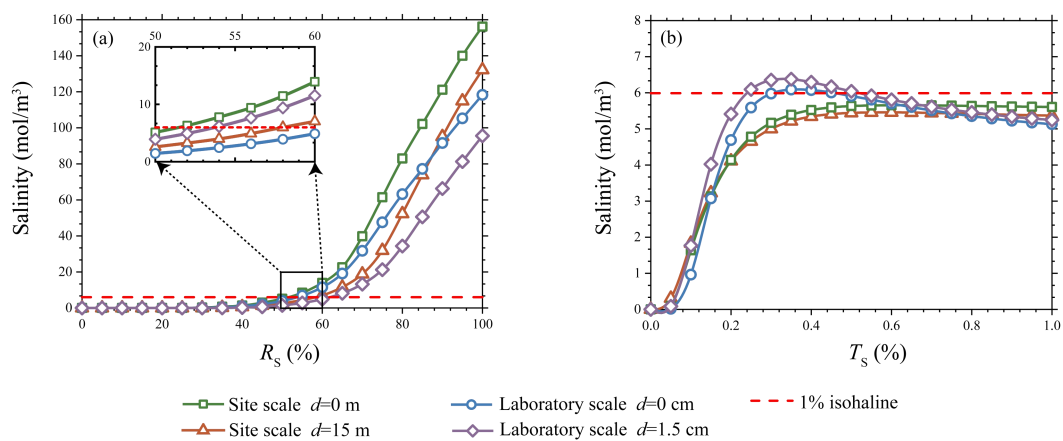
306 This study examined the migration patterns of two synthetic nanoplastics  
307 (PS-Pd-1 and PS-Pd-2) that exhibit contrasting hydrophobicity. The detailed synthesis  
308 protocols are available in Supplementary Materials (Text S2). To ensure model  
309 accuracy, migration parameters for nanoplastics in quartz sand (Table 1) were  
310 validated using column experiment data from Liu et al. (20242025). The experimental  
311 setup and methodology are detailed in Text S3 and Fig. S1, with calibration processes  
312 and results illustrated in Fig. S2 and S3. The primary objective was to quantify how  
313 differential nanoplastic-solid phase interactions influence contamination levels in  
314 freshwater lenses (Amirmoshiri et al., 2020; Wang et al., 2021). As summarized in  
315 Table 1, PS-Pd-1 exhibits strong solid-phase adsorption capacity, whereas PS-Pd-2  
316 demonstrates weaker adsorption. Given potential scale-dependence in nanoplastic  
317 transport parameters, current research remains largely focused on laboratory-scale  
318 investigations (Johnson, 2020; Li et al., 2021; Liu et al., 20242025).

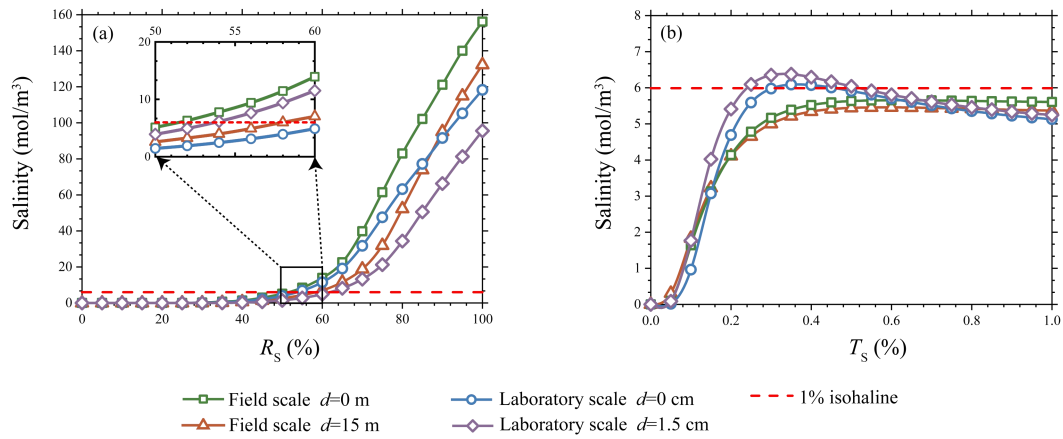
319 A single-well extraction scheme was implemented in the central region of an  
320 idealized strip island aquifer. The maximum safe extraction rate, calculated based on  
321 sharp-interface theory, served as the baseline scenario. However, the applicability of  
322 this theoretical maximum for island freshwater lenses requires critical re-evaluation,  
323 as previous sharp-interface analytical and numerical studies have largely neglected the  
324 transition zone formed by salinity dispersion and diffusion—a factor addressed in  
325 only limited corrections (Coulon et al., 2022). To determine a more accurate  
326 maximum safe extraction rate, a series of numerical simulations with predefined  
327 pumping rates were conducted to calibrate both laboratory-scale and sitefield-scale  
328 conceptual models.

329 Although Tang et al. (2021) provided preliminary numerical validation via Fig.

330 S4(a)(b), their simulations omitted the effects of the unsaturated zone and the salinity  
 331 transition zone. In contrast, our validation-based simulations (Fig. S4(c)(d)), which  
 332 incorporate the unsaturated zone and employ dispersion parameters consistent with  
 333 Chen et al. (20242024b), indicate that the 1% salinity contour exceeds the well  
 334 bottom elevation by 2.03 m. This signifies that pumping-induced salinity surpasses  
 335 regulatory thresholds, necessitating a reduction in extraction volume.

336 The relationship between well salinity and the extraction volume ratio (actual to  
 337 theoretical) in numerical simulations is illustrated in Fig. 3. Results confirm that the  
 338 presence of the unsaturated and transition zones reduces the extraction capacity to  
 339 50% – 60% of the theoretical maximum ( $Q_{Tmax}$ ). Specifically, under laboratory  
 340 conditions, the maximum safe extraction capacity decreased to 61% and 53% of  $Q_{Tmax}$   
 341 for shallow ( $d=0$  cm) and deep ( $d=1.5$  cm) extraction scenarios, respectively (Fig.  
 342 3(a)). Corresponding field-scale simulations showed reductions to 57% and 51% of  
 343  $Q_{Tmax}$  for shallow ( $d=0$  m) and deep ( $d=15$  m) extraction. The temporal evolution of  
 344 well salinity during freshwater lens re-stabilization (Fig. 3(b)) further demonstrates  
 345 that salinity stabilization occurs within 12 minutes at the laboratory scale but requires  
 346 approximately 4.5 years at the field scale, highlighting significant temporal disparities  
 347 influenced by scale effects.





349

350 Fig. 3. Variations in well salinity as a function of the ratio of extraction volume to  
 351 theoretical maximum ( $R_s$ ) and the ratio of time to theoretical equilibrium time ( $T_s$ )  
 352 during pumping at different depths in numerical simulations, measured at both field  
 353 and laboratory scales: (a) Well salinity versus extraction volume, with the magnified  
 354 region indicating the extraction volume range where well concentration approaches  
 355 the 1% isohaline; (b) Temporal concentration variations for wells with salinity near  
 356 the 1% isohaline in panel (a).

### 357 3. Results and Discussion

#### 358 3.1 Distribution Patterns of Nanoplastics Under Pumping Conditions

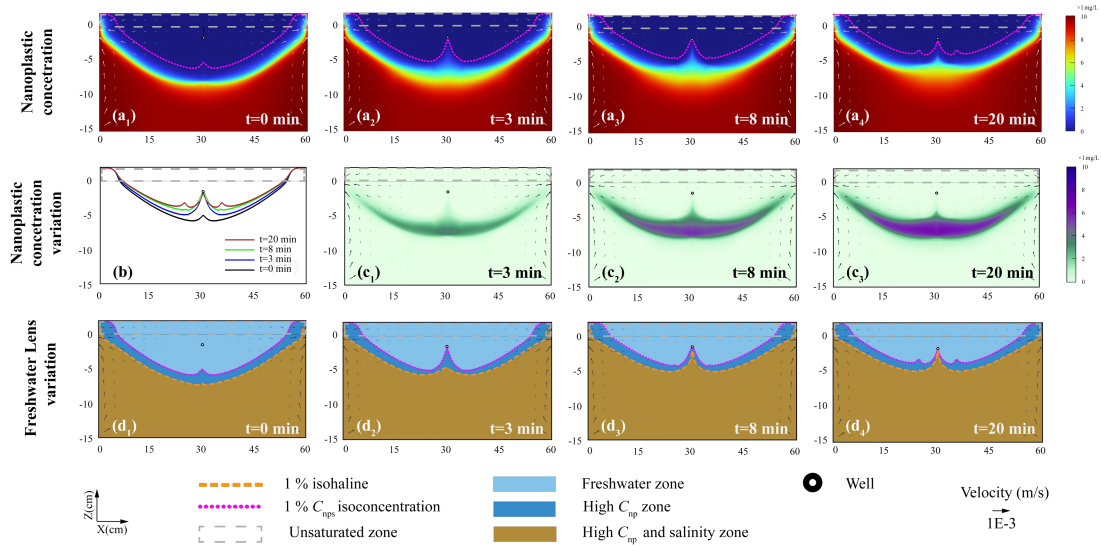
359 Hydrophobic microplastics/nanoplastics (NPs) were selected as the primary  
 360 research focus of this study. Text S4 and Fig. S5 demonstrate that hydrophobic  
 361 molecules/nanoplastic particles exhibit higher mobility and pose more significant  
 362 hazards than hydrophilic counterparts under simulated single-well pumping  
 363 conditions.

364 Fig. 4(a<sub>1</sub>-a<sub>4</sub>) illustrates an “upper cone” phenomenon in nanoplastic  
 365 concentrations during pumping, analogous to that of salinity. Fig. 4(a<sub>1</sub>) reveals that  
 366 highly dispersive nanoplastics may form anomalous distributions in the central  
 367 banded region of the island—a zone previously referred to as the “stagnation zone”  
 368 (Wang et al., 2023). Nearshore aquifers on both sides of the island undergo intense  
 369 convection, driven by groundwater discharge to the sea and seawater intrusion

370 induced by density currents. At the laboratory scale, this convective zone spans  
371 approximately 10 cm; at the field scale, it extends to around 100 meters, where  
372 groundwater Darcy velocities exceed  $1 \times 10^{-3}$  m/s. In contrast, velocities within the  
373 central “stagnation zone” remain below  $1 \times 10^{-8}$  m/s. This zone is dominated by weak  
374 convection, with material transport in groundwater primarily governed by dispersion  
375 and interactions with the solid phase.

376 Fig. 4(b) presents dynamic nanoplastic isoconcentration lines at the wellhead,  
377 where concentrations first increase and then decrease—indicating that wellhead  
378 nanoplastics are influenced by the “stagnation zone”. The discrepancy in migration  
379 behavior between nanoplastics and dissolved solutes stems primarily from their  
380 distinct physicochemical properties: as colloidal particles, nanoplastic migration is  
381 regulated not only by advection-dispersion but also by particle-medium interactions  
382 (e.g., adsorption-desorption, clogging, and filtration). Fig. 4(c<sub>1</sub>-c<sub>3</sub>) depicts variations  
383 in nanoplastic concentrations. ~~Nanoplastics—extracted—from~~ Considering the  
384 ~~well~~ nanoplastic concentration threshold resulted in an additional 37.48% reduction in  
385 the ~~initial~~ usable freshwater lens area, while the maximum depth of freshwater ~~bodies-~~  
386 ~~surrounded~~ zones affected by ~~nanoplastics~~ nanoplastic contamination increased by  
387 0.030 m.

388 Fig. 4(d<sub>1</sub>-d<sub>4</sub>) compares the distribution patterns of salinity and nanoplastics,  
389 revealing that nanoplastics exceeding 1% of the critical nanoplastic concentration  
390 ( $C_{nps}$ ) are concentrated within freshwater lens layers. With the disappearance of the  
391 original “stagnation zone”, a new flow field transition zone is formed, triggering the  
392 emergence of a new “stagnation zone”. The proportion of the freshwater lens  
393 occupied by the nanoplastic transition zone (dark blue areas in Fig. 4(d<sub>1</sub>-d<sub>4</sub>)) increased  
394 from 30.27% to 41.24%. Compared to dissolved solutes, nanoplastics possess larger  
395 hydrodynamic diameters and unique surface properties, leading to distinctive  
396 migration patterns in porous media.



397

398 Fig. 4. Distribution and concentration dynamics of PS-Pd-2 hydrophobic nanoplastics  
 399 and corresponding freshwater lens alterations at the laboratory scale (60 cm×17 cm)  
 400 during pumping ( $R_S = 53\%$ ); in numerical simulations: (a<sub>1</sub>-a<sub>4</sub>) freshwater lenses  
 401 demarcated by the 1% isoconcentration line of PS-Pd-2 hydrophobic nanoplastics at 0,  
 402 3, 8 and 20 minutes post-pumping, (b) temporal variation of the 1%  $C_{nps}$   
 403 isoconcentration line, (c<sub>1</sub>-c<sub>3</sub>) net concentration variations relative to the baseline (0  
 404 min) at 3, 8 and 20 minutes post-pumping, (d<sub>1</sub>-d<sub>4</sub>) spatial offset between the 1%  
 405 isohaline and 1%  $C_{nps}$  isoconcentration line around the freshwater lens.

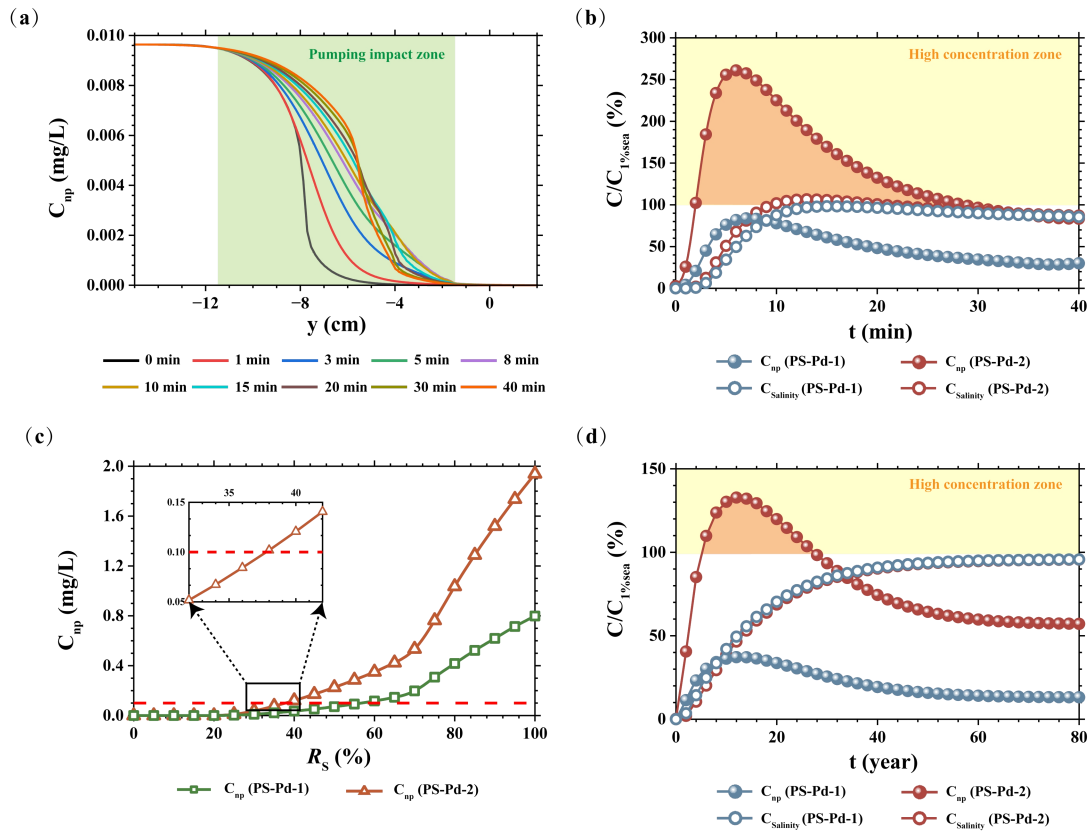
406 Fig. 5(a) presents the vertical concentration profile of nanoplastics at the  
 407 wellhead, further validating the aforementioned mechanism. Prior to pumping  
 408 initiation, the nanoplastic transition zone was situated 0.07 - 0.10 m below the well  
 409 bottom. Following pumping initiation, the transition zone underwent a rapid upward  
 410 migration and expansion to 0.02 m below the well bottom. Thirty minutes  
 411 post-pumping, although the transition zone exhibited a slight recession, a stable  
 412 transition zone was maintained at 0.06 m below the well bottom, while a new steep  
 413 transition zone formed at 0.03 m. nanoplastic Nanoplastic concentrations at the  
 414 wellhead increased markedly within the first 4 minutes, started to decline after 8  
 415 minutes, stabilized at 30 minutes post-pumping, and ultimately converged with the  
 416 concentration trends of chloride (Cl<sup>-</sup>), indicating that solute and colloidal transport are

417 governed primarily by convection. The observed transport behavior can be interpreted  
418 through the lens of effective dispersion parameters. In porous media transport  
419 modeling, the macroscopic dispersion coefficient in advection-dispersion equations  
420 serves as an effective parameter that implicitly captures the integrated effects of  
421 various pore-scale processes, including particle-pore interactions, flow path tortuosity,  
422 and temporary retention at pore throats. While these microscopic processes are not  
423 explicitly resolved in the current continuum-scale model, their integrated effects are  
424 reflected in the calibrated dispersion parameters.

425 Fig. 5(b) illustrates the ~~dynamic~~temporal concentration ~~dynamics~~variations of  
426 hydrophilic and hydrophobic nanoplastics, both of which exhibit an initial increase  
427 followed by a subsequent decrease. During the initial pumping phase (0 - 6 min),  
428 high-concentration nanoplastics in the immediate vicinity of the well were the  
429 primary fraction extracted by pumping, leading to a sharp concentration increase to a  
430 peak of 2.489%  $C_{nps}$ . With prolonged pumping (6 - 32 min), peripheral groundwater  
431 with relatively low-nanoplastic ~~peripheral groundwater concentrations~~ gradually  
432 ~~infiltrated~~entered the pumping-affected zone. The original stagnation zone was  
433 reconfigured under the influence of pumping, with new stagnation zones emerging on  
434 both sides of the well. The system eventually attained a state of dynamic equilibrium  
435 after 32 min of pumping, with nanoplastic concentrations stabilizing at a steady level.  
436 Notably, salinity variations under distinct contamination scenarios involving  
437 hydrophilic and hydrophobic nanoplastics also ~~exerted a notable regulatory influence~~  
438 ~~on~~influenced this process. This phenomenon is hypothesized to originate from an  
439 approximate 40% reduction in hydraulic conductivity, which is induced by the  
440 solid-phase enrichment of hydrophilic nanoplastics in specific central regions of the  
441 study domain.

442 With respect to the distinct distribution characteristics of wellborne hydrophobic  
443 nanoplastics presented in Fig. 5(b), which diverge from those of salinity, the  
444 application of a 1% concentration threshold to nanoplastics (consistent with the  
445 salinity threshold) results in wellhead nanoplastic concentrations exceeding this

446 criterion for more than 80% of the duration prior to the attainment of a stable system  
447 state. To mitigate the adverse impacts of the extensive dispersion of hydrophobic  
448 nanoplastics on the quality of pumped groundwater, Fig. 5(c) ~~presentss~~shows the  
449 ~~correlations~~relationships between ~~hydrophilic and hydrophobic wellhead~~ nanoplastic  
450 concentrations ~~at the wellhead~~ and ~~the~~ cumulative pumped water volume ~~for~~  
451 ~~hydrophilic and hydrophobic nanoplastics~~. Under the theoretical maximum safe  
452 pumping rate, hydrophobic nanoplastics accumulate at the wellhead to a concentration  
453 of 1.939 mg/L during the initial pumping phase. To reduce the initial wellhead  
454 nanoplastic concentrations to below the 1%  $C_{nps}$  threshold, the actual maximum safe  
455 pumping rate must be further reduced to 37% of the theoretical maximum safe  
456 pumping rate. Fig. 5(d) ~~verifies~~indicates that ~~this identical a~~ similar phenomenon is  
457 observable in wellhead nanoplastic concentrations at the field scale, where  
458 nanoplastics at such concentrations are still rapidly entrained into the pumping  
459 well—indicating that the enrichment mechanism driven by high nanoplastic  
460 dispersibility remains valid at the field scale. High-concentration nanoplastic influxes  
461 at the wellhead persisted ~~over a~~from years 5– ~~to~~ 28-year timeframe at the field scale.  
462 Conversely, nanoplastic concentrations in the upper cone region are comparatively  
463 lower, with those in the island ’ s pumping wells reaching only 1.329-%  $C_{nps}$ . A  
464 detailed elucidation of the underlying mechanisms for this phenomenon is presented  
465 in Section 3.2.



466

467 Fig. 5. Concentration dynamics at laboratory and field scales and their responses to

468 pumping rate adjustments in numerical simulations: (a) 1%  $C_{nps}$  isoconcentration line

469 variation along the central axis ( $x=30$  cm) at laboratory scale; (b) Temporal variations

470 in salinity and nanoplastic concentrations for hydrophilic and hydrophobic

471 nanoplastics at laboratory scale; (c) Well nanoplastic concentration as a function of

472 pumped volume-to-theoretical maximum ratio ( $R_s$ ) for groundwater nanoplastics of

473 distinct hydrophilic-hydrophobic properties; (d) Temporal variations in well salinity

474 and nanoplastic concentrations for hydrophilic and hydrophobic nanoplastics at field

475 scale.

### 476 3.2 Scale Effects on Nanoplastic Transport

477 In field-scale simulations, the background concentration of hydrophobic

478 nanoplastics was set to  $1 \mu\text{g/L}$  ( $C_{nps}$ ). Dispersion parameters were adjusted based on

479 scaling-up experience (Gelhar et al., 1992), with the corresponding simulation results

480 presented in Fig. 6. Fig. 6(a<sub>1</sub>) shows that following stabilization of the freshwater lens,

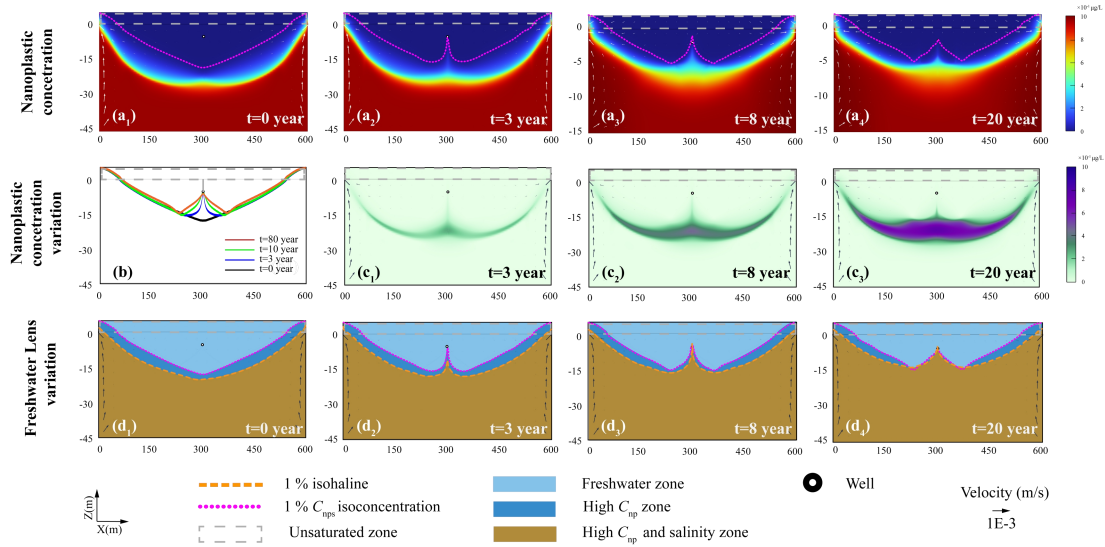
481 the 90%–10%  $C_{nps}$  transition zone in the central island region thickened to more than

482 10 m, yet no prominent dispersion-driven upward cone formed in the island's core

483 area. Scale effects exert their influence primarily in two aspects: with increasing scale,  
484 the heterogeneity of the aquifer medium becomes more complex, which may mask the  
485 unique migration behavior of nanoplastics. Additionally, streamline curvature is  
486 reduced and flow velocity distributions are more homogeneous at larger scales,  
487 thereby ~~attenuating inertial effects~~reducing the influence of local streamline curvature  
488 on particle migration.

489 Upon pumping initiation at the field scale, the depth of the freshwater lens  
490 decreased from 20.168 m to 13.785 m, while the maximum depth of the freshwater  
491 lens encircled by nanoplastics decreased from 17.943 m to 14.610 m. Fig. 6(c<sub>1</sub>-c<sub>3</sub>)  
492 depicts variations in nanoplastic concentration within the lens: the volumetric fraction  
493 of nanoplastics occupying the freshwater lens decreased from 31.48% to 23.40%, a  
494 trend that deviates from the increasing pattern observed at the laboratory scale. Fig.  
495 6(d<sub>1</sub>-d<sub>4</sub>) reveals the existence of a ~3 m-thick residual ~~dissolved~~nanoplastic-bearing  
496 layer within the freshwater lens, with concentrations at 1-5% of the nanoplastic  
497 concentration in seawater. Upon stabilization of pumping, the transition zone migrated  
498 upward toward the ~~bilateral jet~~lateral high-velocity discharge zones but no new  
499 upward cone was generated. At the field scale, the enhancement of nanoplastic  
500 dispersion relative to solute dispersion was no longer pronounced, a phenomenon  
501 likely due to improved flow stability and inherent scale effects. In addition, the  
502 residence time of colloidal filtration and entrainment processes is extended at this  
503 scale, which may consequently modify the final spatial distribution of nanoplastics.

504



505

506 Fig. 6. Hydrophobic nanoplastic concentration dynamics and corresponding  
 507 freshwater lens alterations at field scale (600 m×50 m) during pumping ( $R_S = 51\%$ )  
 508 in numerical simulations: (a<sub>1</sub>-a<sub>4</sub>) Freshwater lenses demarcated by the 1% PS-Pd-2  
 509 nanoplastic isoconcentration line at 0, 3, 8 and 20 years post-pumping; (b) 1%  $C_{nps}$   
 510 isoconcentration line variation; (c<sub>1</sub>-c<sub>3</sub>) Net nanoplastic concentration variations  
 511 relative to the initial time point (0 year) at 3, 8 and 20 years post-pumping; (d<sub>1</sub>-d<sub>4</sub>)  
 512 Spatial offset between the 1% isohaline and 1%  $C_{nps}$  isoconcentration line around the  
 513 freshwater lens.

### 514 3.3 Sensitivity Analysis

515 Four factors were selected for analysis, with the  $VR$ ,  $ASYR$ , and  $RRSY$  metrics  
 516 employed to evaluate nanoplastic contamination in freshwater and freshwater lenses,  
 517 as well as its implications for pumping operations.

518 Fig. 7(a<sub>1</sub>, b<sub>1</sub>) demonstrates that dispersion nanoplastic dispersivity exhibits a  
 519 significant correlation with  $VR$ , and nanoplastic dispersivity exerts a notable influence  
 520 on pumping efficiency. When nanoplastic dispersivity is lower than that of solutes, the  
 521 distribution range of nanoplastics closely approximates that of solutes, resulting in a  
 522 narrow transition zone, while  $Q_{Amax}$  is exclusively governed by salinity. When  
 523 nanoplastic dispersivity equals that of solutes, the nanoplastic-constrained freshwater  
 524 lens zone formed by nanoplastics nearly perfectly overlaps with the seawater-enclosed

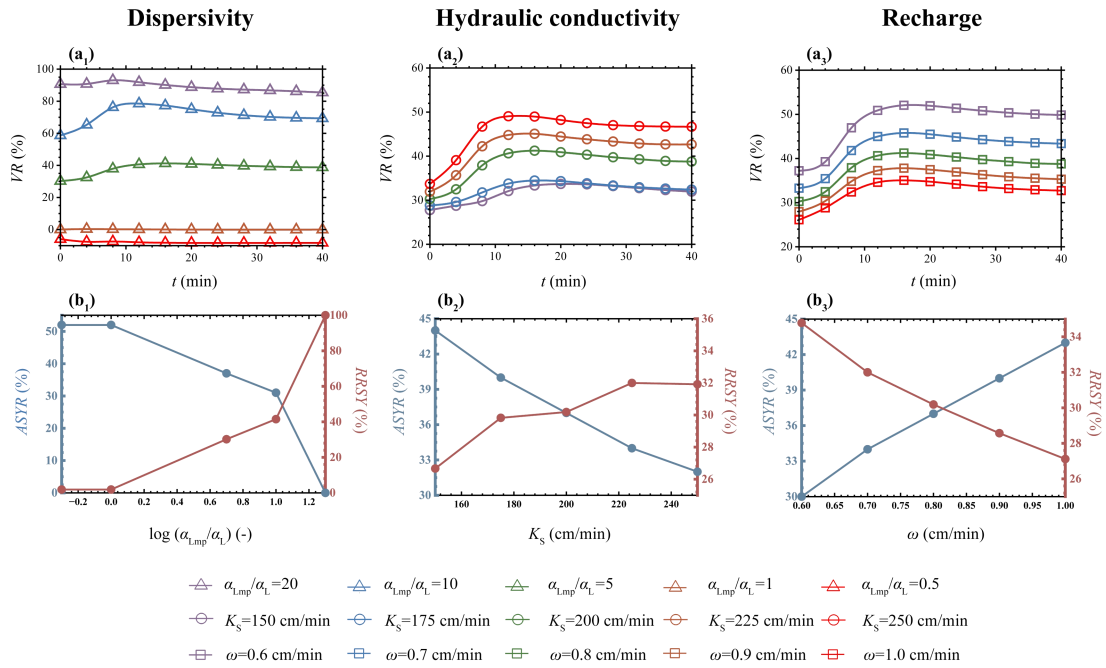
525 ~~area~~salinity-defined freshwater lens zone. As dispersivity increases to 10 times that of  
526 solutes, the volume of freshwater lenses decreases by approximately 30%. When the  
527 effective dispersivity of ~~residual~~—nanoplastics exceeds 17 times that of  
528 salinitydissolved salts, the expanded dispersion range causes the 1%  $C_{nps}$   
529 isoconcentration line to cover the wellhead area. The high sensitivity of nanoplastic  
530 behavior to dispersivity stems from their particulate nature: nanoplastics migrate not  
531 only via hydraulic dispersion but also through mechanisms such as Brownian motion,  
532 gravitational settling, and media interception. High dispersivity reflects the selective  
533 migration capacity of nanoplastics within complex pore structures, which is closely  
534 associated with their surface properties and hydrodynamic characteristics.

535 Fig. 7(a<sub>2</sub>,b<sub>2</sub>) reveals that  $VR$  gradually increases with rising hydraulic  
536 conductivity. At a hydraulic conductivity of 250 cm/min, 46.68% of the freshwater  
537 lens area is occupied by high-concentration nanoplastics. Under pumping conditions,  
538 both high hydraulic conductivity and high-permeability media result in a significant  
539 reduction in the usable portion of freshwater lens layers surrounded by nanoplastics.  
540 Aquifer hydraulic conductivity is another critical parameter regulating solute  
541 migration and retention. Previous studies have demonstrated that higher hydraulic  
542 conductivities result in reduced freshwater lens volumes and correspondingly  
543 decreased groundwater availability (Bailey and Jenson, 2014; Cui et al., 2021; Gao et  
544 al., 2025). The spatial distribution and magnitude of freshwater lenses surrounded by  
545 nanoplastics are consistent with these findings. High hydraulic conductivity  
546 accelerates freshwater discharge on both sides of the island, reducing the area where  
547 freshwater lenses can maintain equilibrium. For nanoplastics, increased hydraulic  
548 conductivity enhances flow velocity and convective transport capacity, thereby  
549 facilitating their intrusion into freshwater lenses.

550 Recharge rates were used to ~~simulate precipitation intensity~~represent effective  
551 rainfall infiltration on the island. Fig. 7(a<sub>3</sub>) shows that ~~precipitation~~recharge  
552 significantly reduces the spatial distribution density of nanoplastics within freshwater  
553 lenses, with this effect being pronounced both before and after pumping. Increased

554 recharge leads to a decrease in  $VR$ ; when recharge rises to 1.0 cm/min,  $VR$  declines to  
555 33%. Conversely, when recharge drops below 0.65 cm/min, the final variation in  $VR$   
556 also weakens, suggesting that nanoplastic concentrations are more difficult to mitigate  
557 with increased pumping intensity. Fig. 7(b<sub>3</sub>) illustrates that enhanced recharge reduces  
558 the volume occupied by high-concentration nanoplastics in freshwater lenses,  
559 significantly increasing exploitable freshwater volume and alleviating the impact of  
560 nanoplastics on maximum safe pumping rates. Previous studies indicate that the  
561 volume and thickness of island freshwater lenses are positively correlated with  
562 precipitation (Zheng et al., 2025). The "flushing effect" of precipitationrecharge on  
563 nanoplastic distribution likely operates through two mechanisms: first,  
564 precipitationrecharge acts as the main source of freshwater storage in lenses. As the  
565 freshwater lens area expands, the thick transition zone formed by hydrophobic  
566 nanoplastics remains unaffected by convection and maintains a constant thickness,  
567 leading to a reduced proportion of nanoplastics despite unchanged total volume.  
568 Second, increased recharge may expand the strong convection zones on both sides of  
569 the seawater boundary, shrinking the central "stagnation zone" and thereby relatively  
570 weakening dispersion effects.

571       Among the analyzed media and environmental conditions, dispersivity emerges  
572 as the key parameter governing nanoplastic retention behavior in freshwater lenses,  
573 with high dispersivity exerting the most pronounced inhibitory effect on  $Q_{Amax}$ .



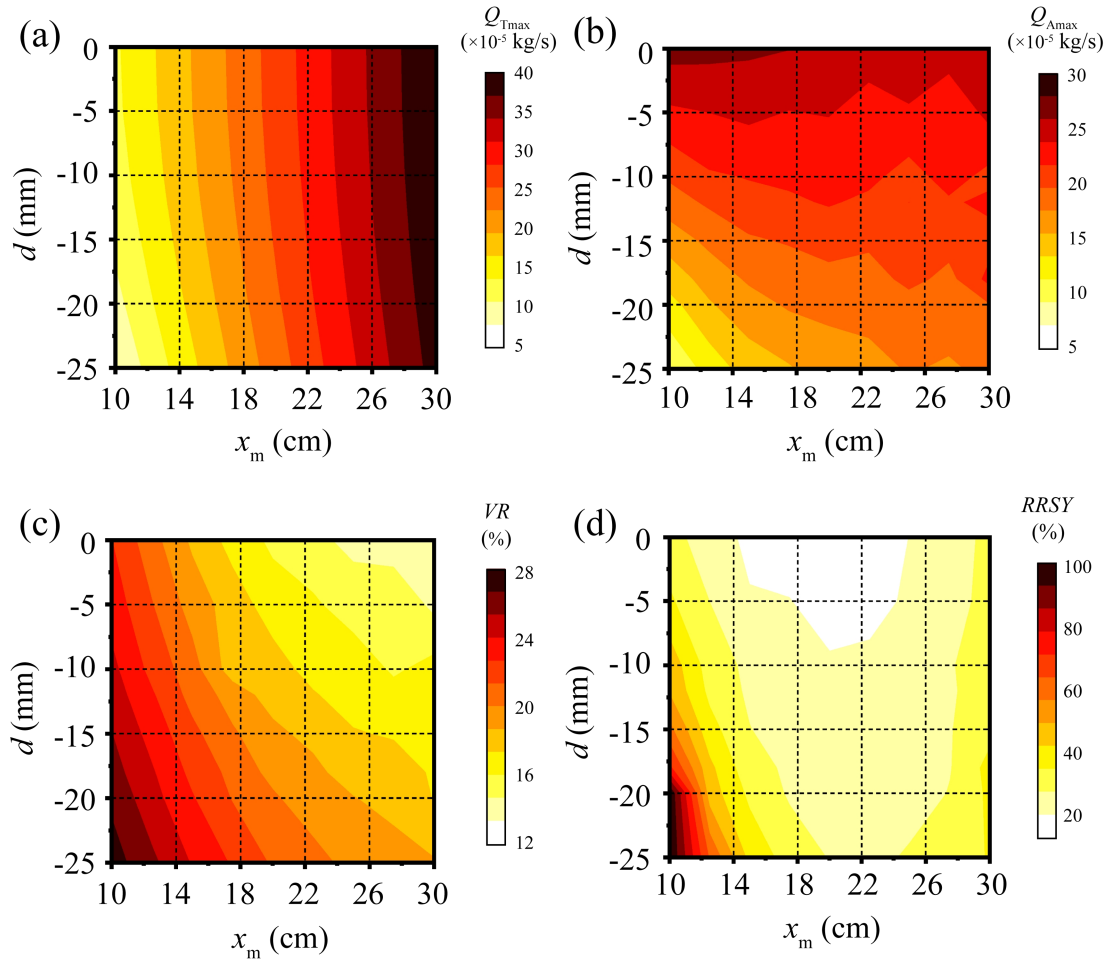
574

575 Fig. 7. The volume reduction rate of freshwater lenses ( $VR$ ), the ratio of actual  
 576 maximum safe extraction capacity to theoretical maximum safe extraction capacity  
 577 ( $ASYR$ ), and the ratio of maximum safe extraction capacity reduction due to  
 578 nanoplastic retention to maximum safe extraction capacity ( $RRSY$ ) versus (a<sub>1</sub>-a<sub>3</sub>)  
 579 dispersivity, (b<sub>1</sub>-b<sub>3</sub>) hydraulic conductivity, and (c<sub>1</sub>-c<sub>3</sub>) recharge rate in numerical  
 580 simulations.

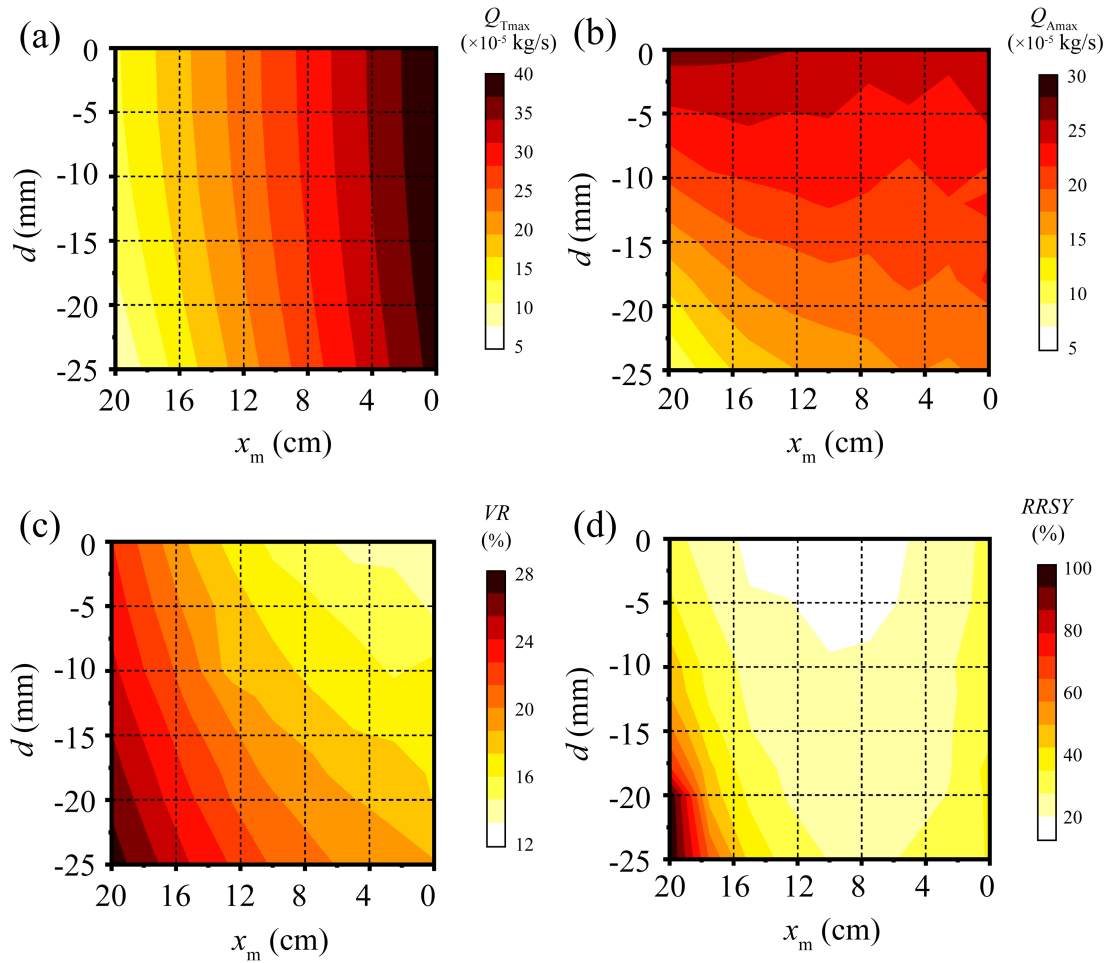
581 Fig. 8(a) and (b) present the theoretically derived maximum safe pumping rate  
 582 near the freshwater lens center (Tang et al., 2021) and the actual maximum safe  
 583 pumping rate, respectively. Under standard pumping conditions, the presence of a  
 584 transition zone reduces the effective area of the freshwater lens by 16.12% and its  
 585 thickness by 7.77 m. The position of pumping wells directly influences pumping rates:  
 586 as the distance from the central region increases, pumping rates decrease linearly, as  
 587 expressed in Equation (405). Simulation results demonstrate that the maximum safe  
 588 pumping rate of freshwater lenses does not exhibit a perfect linear correlation with the  
 589 distance from the surface central axis. During shallow pumping, higher rates may  
 590 even be achieved near the coastal sides due to the low-velocity zone in the center. The  
 591 Under salinity-based constraints, the actual maximum safe pumped volume occurs at  
 592  $x=10$ the pumping point ( $x_m=20$  cm,  $y=0$  cm), corresponding to approximately

593 two-thirds of the ~~island's half-width~~ of the island from the central axis, with a  
594 pumping rate of  $2.667 \times 10^{-5}$  kg/s (200% of the theoretical value). At the center, the  
595 rate decreases to  $2.480 \times 10^{-5}$  kg/s, equivalent to 62% of the theoretical value. Under  
596 idealized strip-shaped island hydrodynamic conditions, seawater infiltrates from both  
597 bottom sides, forming an outflow zone at the top of the coastline, with a "stagnation  
598 zone" emerging in the island center—a phenomenon confirmed in previous studies.  
599 Owing to the slow, predominantly vertical flow in the central region, residual brackish  
600 water persists and disperses upward primarily via vertical dispersion. Thus, for  
601 single-well pumping projects on small idealized strip-shaped islands, central pumping  
602 may not be optimal, whereas lateral single-well operations can yield higher freshwater  
603 outputs. For deep pumping, given that freshwater lenses on such islands are  
604 approximately semicircular, deeper pumping is feasible near the center.

605 Fig. 8(c) illustrates that nanoplastic concentration constraints reduce freshwater  
606 lens volume by 13-28%, with more significant reductions in areas farther from the  
607 island's surface central axis, attributed to the uneven distribution of the nanoplastic  
608 transition zone. With respect to the reduction in maximum safe pumping rates, Fig.  
609 8(d) demonstrates the decline in pumped volumes at the island center when  
610 nanoplastic concentration limits are considered. Centered at the pumping point  
611 (~~x=20~~x<sub>m</sub>=10 cm, y=0 cm), the maximum safe pumped volume gradually decreases  
612 with increasing distance from this center due to nanoplastic concentration restrictions.  
613 Near the seawater boundary, the transition zone completely covers the area within 10  
614 cm of the shoreline. Under the 1%  $C_{nps}$  concentration limit, regions deeper than 25  
615 mm are designated as non-exploitable zones. This phenomenon arises because the  
616 nanoplastic transition zone is relatively extended in the island's central region. Certain  
617 central regions exhibit pathway advantages, facilitating faster nanoplastic  
618 accumulation into wells. Near the seawater boundary, exploitable volumes decrease  
619 due to the influence of seawater nanoplastic source concentrations. Consequently, the  
620 combined effect of these two factors results in the highest exploitable volumes  
621 occurring in the upper regions near the central axis.



622



623

624 Fig. 8. Combined effectsEffects of pumping depth ( $d$ ) and shore horizontal distance  
 625 from the island center ( $x_m$ ) on (a) theoretical maximum safe extraction capaeityrate  
 626 ( $Q_{Tmax}$ ), (b) actual maximum safe extraction capaeityrate ( $Q_{Amax}$ ), (c) freshwater lens  
 627 volume reduction rate ( $VR$ ), and (d) thereduction ratio of maximum safe extraction  
 628 capaeity reduction due to yield caused by nanoplastic retention to maximum safe  
 629 extraction capacity (RRSY) in the idealized strip-island aquifer.

630

#### 631 4. Conclusion

632 This study established a coupled variable-density groundwater flow and transport  
 633 model to explore nanoplastic migration in the freshwater lenses of idealized strip  
 634 islands under pumping scenarios. By integrating laboratory-calibrated parameters

635 with field-scale simulations, we ~~identify~~identified fundamental differences between  
636 nanoplastic and traditional solute transport processes and ~~evaluate~~evaluated their  
637 implications for groundwater management in island aquifers. Key conclusions are  
638 summarized as follows:

639 (1) Nanoplastic transport differs fundamentally from dissolved salt transport  
640 within the freshwater lenses of idealized strip-island aquifers during groundwater  
641 pumping. In contrast to dissolved salts, whose behavior is mainly regulated by  
642 advection and dispersion, nanoplastics are further affected by particle-specific  
643 processes, such as adsorption-desorption, clogging, and filtration. The higher effective  
644 dispersivity leads to earlier breakthrough at extraction wells and the development of  
645 broader contaminant transition zones compared to salinity alone under  
646 pumping-induced upconing conditions in coastal island aquifers.

647 (2) Transport behavior exhibits strong scale dependence in strip-island  
648 freshwater lens systems under pumping stress. Laboratory-scale simulations showed  
649 rapid contamination and prominent "upper cone" formation within minutes, whereas  
650 field-scale simulations demonstrated attenuated upward coning and much longer  
651 stabilization times on the order of years. This contrast highlights the importance of  
652 multi-scale modeling when extrapolating experimental results to real-world island  
653 aquifers subject to freshwater extraction and seawater intrusion.

654 (3) Dispersivity is the dominant control on nanoplastic risk for pumping wells  
655 tapping freshwater lenses in strip-island coastal aquifers. Among the evaluated  
656 parameters, nanoplastic dispersivity exerts the strongest influence on contaminant  
657 accumulation in extraction wells, with hydraulic conductivity and recharge rates  
658 playing secondary but important roles. When nanoplastic dispersivity exceeds  
659 approximately 17 times that of dissolved solutes, the contaminant plume can fully  
660 envelop the well screen, reducing the maximum safe extraction rate ~~by~~to 37-50%  
661 ~~compared to~~of the salinity-based thresholds under island pumping scenarios.

662 (4) Well placement strategies must account for nanoplastic transition zones.

663 Traditional guidelines based solely on salinity intrusion may not minimize  
664 contamination risks. Simulations suggest that central pumping locations are not  
665 always optimal; lateral well placement (~~approximately two-thirds of the distance from~~  
666 ~~the island centerline~~) can increase freshwater yield ~~while reducing, although the~~  
667 optimal position depends on whether salinity or nanoplastic ~~contamination~~  
668 potential concentration is used as the limiting criterion.

669 Several simplifying assumptions were adopted in this study, including  
670 homogeneous aquifer properties, idealized boundary conditions, and limited  
671 representation of nanoplastic diversity. In practice, aquifer heterogeneity, tidal  
672 fluctuations, and storm events, ~~and~~ may further influence the wide  
673 range groundwater flow field and, consequently, the transport of substances.  
674 Furthermore, the diverse properties of environmental ~~nanoplastic properties,~~  
675 including nanoplastics such as particle size distribution, aging state, and surface  
676 chemistry, ~~may further influence transport behavior. Moreover will also bring~~  
677 additional impacts on their migration. In addition, only two ~~synthetic nanoplastic~~  
678 types of synthetic nanoplastics were considered herein this study, whereas natural  
679 systems contain a broader and more complex spectrum of particles. Despite these  
680 limitations, the present study establishes a mechanistic framework for evaluating  
681 nanoplastic transport in coastal freshwater lenses. By coupling variable-density flow  
682 with particle-specific transport processes and quantifying impacts on safe extraction  
683 thresholds, this study provides a process-based basis clear practical implications for  
684 revising well design, pumping optimization, and groundwater management ~~strategies~~  
685 in island settings on small islands. Future research should ~~incorporate perform~~  
686 heterogeneous aquifer structures, simulations, consider dynamic ~~hydrological forcing,~~  
687 and broader tidal and sea-level rise scenarios, and adopt more realistic natural  
688 micro/nanoplastic characteristics properties to ~~enhance predictive capability and~~  
689 support further improve prediction accuracy and practical applicability for water  
690 security in increasingly plastic-polluted coastal environments.

691 **Data availability**

692 The data of this study can be found in Zheng (2026,  
693 <https://zenodo.org/records/19150343> ).

694 **Author contributions**

695 TYZ: Conceptualization, Writing-Original Draft, Methodology, Resources,  
696 Writing-Review and Editing, Funding acquisition, Supervision.

697 CXM: Investigation, Software, Writing-Original Draft, Writing-Review and Editing,  
698 Visualization, Data Curation, Conceptualization.

699 SBG: Methodology, Formal Analysis, Investigation, Visualization, Writing-Review  
700 and Editing.

701 JL: Writing-Review and Editing, Methodology, Supervision, Conceptualization.

702 **Competing interests**

703 The contact author has declared that none of the authors has any competing interests.

704 **Financial support**

705 This work was supported by the National Natural Science Foundation of China (No.  
706 42422207), Taishan Scholars Program of Shandong Province (No. tsqn202408078)  
707 and the Postdoctoral Fellowship Program of CPSF under Grant Number  
708 GZC20250290.

709

710 **Reference**

## 711 References

- 712 Abdoulhalik, A., & Ahmed, A. A. (2018), Transient investigation of saltwater upconing in  
713 laboratory-scale coastal aquifer, *Estuarine, Coastal and Shelf Science*, 214, 149-160.  
714 <https://doi.org/10.1016/j.ecss.2018.09.024>.
- 715 Al Harraq, A., & Bharti, B. (2022), Microplastics through the Lens of Colloid Science, *ACS*  
716 *Environmental Au*, 2(1), 3-10. <https://doi.org/10.1021/acsenvironau.1c00016>.
- 717 Alkindi, A., Al-Wahaibi, Y., Bijeljic, B. & Muggeridge, A. (2011), Investigation of longitudinal  
718 and transverse dispersion in stable displacements with a high viscosity and density contrast  
719 between the fluids. *Journal of Contaminant Hydrology*, 120-121, 170-183.  
720 <https://doi.org/10.1016/j.jconhyd.2010.06.006>.
- 721 Alsumaiei, A. A., & Bailey, R. T. (2018), Quantifying threats to groundwater resources in the  
722 Republic of Maldives Part I: Future rainfall patterns and sea-level rise, *Hydrological*  
723 *Processes*, 32(9), 1137-1153. <https://doi.org/10.1002/hyp.11480>.
- 724 Amirmoshiri, M., Zhang, L., Puerto, M. C., Tewari, R. D., Bahrim, R. Z. B. K., Farajzadeh, R.,  
725 Hirasaki, G. J., & Biswal, S. L. (2020), Role of Wettability on the Adsorption of an Anionic  
726 Surfactant on Sandstone Cores, *Langmuir*, 36(36), 10725-10738.  
727 <https://doi.org/10.1021/acs.langmuir.0c01521>.
- 728 Babakhani, P., Bridge, J., Doong, R. A., & Phenrat, T. (2017), Continuum-based models and  
729 concepts for the transport of nanoparticles in saturated porous media: A state-of-the-science  
730 review, *Advances in colloid and interface science*, 246, 75-104.  
731 <https://doi.org/10.1016/j.cis.2017.06.002>.
- 732 Babu, R., Park, N., & Nam, B. (2020), Regional and well-scale indicators for assessing the  
733 sustainability of small island fresh groundwater lenses under future climate conditions,  
734 *Environmental Earth Sciences*, 79(1), 47. <https://doi.org/10.1007/s12665-019-8773-3>.
- 735 Bailey, R. T., & Jenson, J. W. (2014), Effects of Marine Overwash for Atoll Aquifers:  
736 Environmental and Human Factors, *Groundwater*, 52(5), 694-704.  
737 <https://doi.org/10.1111/gwat.12117>.
- 738 Chen, G., Zou, Y., Xiong, G., Wang, Y., Zhao, W., Xu, X., Zhu, X., Wu, J., Song, F., & Yu, H.  
739 (2024a), Microplastic transport and ecological risk in coastal intruded aquifers based on  
740 a coupled seawater intrusion and microplastic risk assessment model, *Journal of hazardous*  
741 *materials*, 480, 135996. <https://doi.org/10.1016/j.jhazmat.2024.135996>.
- 742 Chen, Q., Zhang, L., Shen, C., & Lu, C. (2024b), Effects of groundwater pumping on pore  
743 water flow and salt transport in tide-controlled unconfined coastal aquifers, *Hydrological*  
744 *Processes*, 38(8), e15261. <https://doi.org/10.1002/hyp.15261>.
- 745 Coulon, C., Lemieux, J. M., Pryet, A., Bayer, P., Young, N. L., & Molson, J. (2022), Pumping  
746 Optimization Under Uncertainty in an Island Freshwater Lens Using a Sharp-Interface  
747 Seawater Intrusion Model, *Water Resources Research*, 58(8), e2021WR031793.  
748 <https://doi.org/10.1029/2021WR031793>.
- 749 Cui, X., Zhu, C., Hu, M., Wang, R., & Liu, H. (2021), Permeability of porous media in coral reefs,  
750 *Bulletin of Engineering Geology and the Environment*, 80(6), 5111-5126.  
751 <https://doi.org/10.1007/s10064-020-02082-5>.
- 752 Dagan, G., & Bear, J. (1968), Solving The Problem Of Local Interface Upconing In A Coastal  
753 Aquifer By The Method Of Small Perturbations, *Journal of Hydraulic Research*, 6(1), 15-44.

754 <https://doi.org/10.1080/00221686809500218>.

755 Dose, E. J., Stoeckl, L., Houben, G. J., Vacher, H. L., Vassolo, S., Dietrich, J., & Himmelsbach, T.  
756 ~~J. J. o. H.~~(2014), Experiments and Modeling of Freshwater Lenses in Layered Aquifers:  
757 Steady State Interface Geometry, Journal of Hydrology, 509, 621-630.  
758 <http://dx.doi.org/10.1016/j.jhydrol.2013.10.010>.

759 Gao, C., Zheng, T., Chang, Q., Zheng, X., Song, X., & Luo, J. (2025), Dynamics of Irregular  
760 Freshwater Lenses Evolution in Thin Aquifers of Reclaimed Circular Islands, *Water*  
761 *Resources Research*, 61(7), e2024WR038880. <https://doi.org/10.1029/2024WR038880>.

762 Gelhar, L. W., Welty, C., & Rehfeldt, K. R. (1992), A critical review of data on field-scale  
763 dispersion in aquifers, *Water Resources Research*, 28(7), 1955-1974.  
764 <https://doi.org/10.1029/92WR00607>.

765 Gonçalves, J. M., & Bebianno, M. J. (2021). Nanoplastics impact on marine biota: A review.  
766 *Environmental Pollution*, 273, 116426. <https://doi.org/10.1016/j.envpol.2021.116426>.

767 Houben, G., & Post, V. E. A. (2017), The first field-based descriptions of pumping-induced  
768 saltwater intrusion and upconing, *Hydrogeology Journal*, 25(1), 243-247.  
769 <https://doi.org/10.1007/s10040-016-1476-x>.

770 Isobe, A., Iwasaki, S., Uchida, K., & Tokai, T. (2019), Abundance of non-conservative  
771 microplastics in the upper ocean from 1957 to 2066, *Nature Communications*, 10(1), 417.  
772 <https://doi.org/10.1038/s41467-019-08316-9>.

773 Johnson, W. P. (2020), Quantitative Linking of Nanoscale Interactions to Continuum-Scale  
774 Nanoparticle and Microplastic Transport in Environmental Granular Media, *Environmental*  
775 *Science & Technology*, 54(13), 8032-8042. <https://doi.org/10.1021/acs.est.0c01172>.

776 Ketabchi, H., Mahmoodzadeh, D., Ataie-Ashtiani, B., Werner, A. D., & Simmons, C. T. (2014),  
777 Sea-level rise impact on fresh groundwater lenses in two-layer small islands, *Hydrological*  
778 *Processes*, 28(24), 5938-5953. <https://doi.org/10.1002/hyp.10059>.

779 Koelmans, A. A., Redondo-Hasselerharm, P. E., Nor, N. H. M., de Ruijter, V. N., Mintenig, S. M. ,  
780 & Kooi, M. (2022), Risk assessment of microplastic particles, *Nature Reviews Materials*,  
781 7(2), 138-152. <https://doi.org/10.1038/s41578-021-00411-y>.

782 Koutnik, V. S., Leonard, J., Alkidim, S., DePrima, F. J., Ravi, S., Hoek, E. M. V., & Mohanty, S. K.  
783 (2021), Distribution of microplastics in soil and freshwater environments: Global analysis  
784 and framework for transport modeling, *Environmental pollution (Barking, Essex : 1987)*, 274,  
785 116552. <https://doi.org/10.1016/j.envpol.2021.116552>.

786 Lee, J., Rolle, M. & Kitanidis, P. (2017), Longitudinal dispersion coefficients for numerical  
787 modeling of groundwater solute transport in heterogeneous formations. *Journal of*  
788 *Contaminant Hydrology*, 212, 41-54. <https://doi.org/10.1016/j.jconhyd.2017.09.004>.

789 Li, J., Liu, H., & Paul Chen, J. (2018), Microplastics in freshwater systems: A review on  
790 occurrence, environmental effects, and methods for microplastics detection, *Water Research*,  
791 137, 362-374. <https://doi.org/10.1016/j.watres.2017.12.056>.

792 Li, M., Zhang, M., Rong, H., Zhang, X., He, L., Han, P., & Tong, M. (2021), Transport and  
793 deposition of plastic particles in porous media during seawater intrusion and  
794 groundwater-seawater displacement processes, *Science of The Total Environment*, 781,  
795 146752. <https://doi.org/10.1016/j.scitotenv.2021.146752>.

796 Liu, Y., Zheng, T., Guo, B., Jiang, S., Cao, X., Zhao, R., Liu, M., Zheng, T., Hao, Y., Wang, C., Liu,  
797 L., Zhao, Y., Liu, Z., Dai, Y., Yue, T., Zhao, J., Wang, Z., & Xing, B. (2025). Transport of

798 [eco-corona coated nanoplastics in coastal sediments. Water research, 284,](#)  
799 [123893.https://doi.org/10.1016/j.watres.2025.123893.](#)M., & Zheng X. (2024), Adsorption  
800 [Characteristics of Dissolved Organic Nitrogen on Aquifer Porous Media: The Role of Media](#)  
801 [Partiele Size, ACS ES&T Water, 4\(5\), 2170-2180.](#)  
802 [https://doi.org/10.1021/acsestwater.3c00815.](#)

803 ~~Moore, C. J., Moore, S. L., Leecaster, M. K., & Weisberg, S. B. (2001), A Comparison of Plastic~~  
804 ~~and Plankton in the North Pacific Central Gyre, Marine Pollution Bulletin, 42(12),~~  
805 ~~1297-1300. https://doi.org/10.1016/S0025-326X(01)00114-X.~~

806 ~~Muskat, M. (1937), The Flow of Fluids Through Porous Media, Journal of Applied Physics, 8(4),~~  
807 ~~274-282. https://doi.org/10.1063/1.1710292.~~

808 ~~Muskat, M. (1938), The flow of homogeneous fluids through porous media, Soil Sci, 46(2), 169.~~  
809 ~~[https://journals.lww.com/soilsci/fulltext/1938/08000/the\\_flow\\_of\\_homogeneous\\_fluids\\_throu](#)~~  
810 ~~[gh\\_porous.8.aspx.](#)~~

811 Ranjan, V. P., Joseph, A., Sharma, H. B., & Goel, S. (2023), Preliminary investigation on effects of  
812 size, polymer type, and surface behaviour on the vertical mobility of microplastics in a  
813 porous media, Science of The Total Environment, 864, 161148.  
814 [https://doi.org/10.1016/j.scitotenv.2022.161148.](#)

815 ~~Reddy, M. S., Shaik, B., Adimurthy, S., & Ramachandraiah, G. (2006), Description of the small~~  
816 ~~plastics fragments in marine sediments along the Alang Sesiya ship-breaking yard, India,~~  
817 ~~Estuarine, Coastal and Shelf Science, 68(3), 656-660.~~  
818 ~~[https://doi.org/10.1016/j.ecss.2006.03.018.](#)~~

819 Ren, Z., Gui, X., Xu, X., Zhao, L., Qiu, H., & Cao, X. (2021), Microplastics in the  
820 soil-groundwater environment: Aging, migration, and co-transport of contaminants - A  
821 critical review, Journal of hazardous materials, 419, 126455.  
822 [https://doi.org/10.1016/j.jhazmat.2021.126455.](#)

823 Ren, Z., Gui, X., Xu, X., Zhao, L., Qiu, H., Wang, X., & Cao, X. (2022), Weathering of  
824 microplastics and their enhancement on the retention of cadmium in coastal soil saturated  
825 with seawater, Journal of hazardous materials, 440, 129850.  
826 [https://doi.org/10.1016/j.jhazmat.2022.129850.](#)

827 Sayre, R., Noble, S., Hamann, S., Smith, R., Wright, D., Breyer, S., Butler, K., Van Graafeiland,  
828 K., Frye, C., Karagulle, D., Hopkins, D., Stephens, D., Kelly, K., Basher, Z., Burton, D.,  
829 Cress, J., Atkins, K., Van Sistine, D. P., Friesen, B., Allee, R., Allen, T., Aniello, P., Asaad, I.,  
830 Costello, M. J., Goodin, K., Harris, P., Kavanaugh, M., Lillis, H., Manca, E., Muller-Karger,  
831 F., Nyberg, B., Parsons, R., Saarinen, J., Steiner, J., & Reed, A. (2019), A new 30 meter  
832 resolution global shoreline vector and associated global islands database for the development  
833 of standardized ecological coastal units, Journal of Operational Oceanography, 12(sup2),  
834 S47-S56. [https://doi.org/10.1080/1755876X.2018.1529714.](#)

835 Sharan, A., Lal, A., & Datta, B. (2021), A review of groundwater sustainability crisis in the Pacific  
836 Island countries: Challenges and solutions, Journal of Hydrology, 603, 127165.  
837 [https://doi.org/10.1016/j.jhydrol.2021.127165.](#)

838 Singh, A., Chauhan, A., & Gaur, R. (2025), A comprehensive review on the synthesis, properties,  
839 environmental impacts, and chemiluminescence applications of polystyrene (PS), Discover  
840 Chemistry, 2(1), 47. [https://doi.org/10.1007/s44371-025-00125-y.](#)

841 Stoeckl, L., & Houben, G. (2012), Flow dynamics and age stratification of freshwater lenses:

842 Experiments and modeling, *Journal of Hydrology*, 458-459, 9-15.  
843 <https://doi.org/10.1016/j.jhydrol.2012.05.070>.

844 ~~Sussarellu, R., Suquet, M., Thomas, Y., Lambert, C., Fabioux, C., Pernet, M. E. J., Le Goïc, N.,~~  
845 ~~Quillien, V., Mingant, C., Epelboin, Y., Corporeau, C., Guyomarch, J., Robbens, J., Paul Pont,~~  
846 ~~I., Soudant, & P., Huvet, A. (2016), Oyster reproduction is affected by exposure to~~  
847 ~~polystyrene microplastics, *Proceedings of the National Academy of Sciences*, 113(9),~~  
848 ~~2430-2435. <https://doi.org/10.1073/pnas.1519019113>.~~

849 Tang, Y., Lu, C., & Luo, J. (2022), An Analytical solution for groundwater lens pumping in a  
850 three-dimensional rectangular island, *Journal of Hydrology*, 617, 128928.  
851 <https://doi.org/10.1016/j.jhydrol.2022.128928>.

852 Tang, Y., Lu, C., & Luo, J. (2024), Optimizing groundwater pumping in small island groundwater  
853 lenses: An analytical approach, *Journal of Hydrology*, 629, 130579.  
854 <https://doi.org/10.1016/j.jhydrol.2023.130579>.

855 Tang, Y., Rathore, S., Lu, C., & Luo, J. (2020), Development of Groundwater Lens for Transient  
856 Recharge in Strip Islands, *Journal of Hydrology*, 590, 125209.  
857 <https://doi.org/10.1016/j.jhydrol.2020.125209>.

858 Tang, Y., Yan, M., Wang, X., Lu, C., & Luo, J. (2021), Experimental and modeling investigation  
859 of pumping from a fresh groundwater lens in an idealized strip island, *Journal of Hydrology*,  
860 602, 126734. <https://doi.org/10.1016/j.jhydrol.2021.126734>.

861 ten Hietbrink, S., Materić, D., Holzinger, R., Groeskamp, S., & Niemann, H. (2025), Nanoplastic  
862 concentrations across the North Atlantic, *Nature*, 643(8071), 412-416.  
863 <https://doi.org/10.1038/s41586-025-09218-1>.

864 Thompson, R. C., Courtene-Jones, W., Boucher, J., Pahl, S., Raubenheimer, K., & Koelmans, A. A.  
865 (2024), Twenty years of microplastic pollution research—what have we learned?, *Science*,  
866 386(6720), ead12746. <https://doi.org/10.1126/science.adl2746>.

867 van Genuchten, M.T. (1980), A Closed-form Equation for Predicting the Hydraulic Conductivity  
868 of Unsaturated Soils. *Soil Science Society of America Journal*, 44: 892-898.  
869 <https://doi.org/10.2136/sssaj1980.03615995004400050002x>.

870 Voss, C., & Provost, A. M. (2002), SUTRA: A model for 2D or 3D saturated-unsaturated,  
871 variable-density ground-water flow with solute or energy transport, Report Rep. 2002-4231.  
872 <https://doi.org/10.3133/wri024231>.

873 Waldschläger, K., & Schüttrumpf, H. (2020), Infiltration Behavior of Microplastic Particles with  
874 Different Densities, Sizes, and Shapes—From Glass Spheres to Natural Sediments,  
875 *Environmental Science & Technology*, 54(15), 9366-9373.  
876 <https://doi.org/10.1021/acs.est.0c01722>.

877 Wang, R., Shu, L., Zhang, R., & Ling, Z. (2023), Determination of Exploitable Coefficient of  
878 Coral Island Freshwater Lens Considering the Integrated Effects of Lens Growth and  
879 Contraction, *Water*, 15(5), 890, ~~doi: 10.3390/w15050890.~~  
880 <https://doi.org/10.3390/w15050890>.

881 Wang, X., Bolan, N., Tsang, D. C. W., Sarkar, B., Bradney, L., & Li, Y. (2021), A review of  
882 microplastics aggregation in aquatic environment: Influence factors, analytical methods, and  
883 environmental implications, *Journal of hazardous materials*, 402, 123496.  
884 <https://doi.org/10.1016/j.jhazmat.2020.123496>.

885 Wang, Z., & Sedighi, M. (2023), Dispersion properties of nanoplastic spheres in granular media at

886 low Reynolds numbers, *Journal of Contaminant Hydrology*, 259, 104244.  
887 <https://doi.org/10.1016/j.jconhyd.2023.104244>.

888 Werner, A. D., Jakovovic, D., & Simmons, C. T. (2009), Experimental observations of saltwater  
889 up-coning, *Journal of Hydrology*, 373(1), 230-241.  
890 <https://doi.org/10.1016/j.jhydrol.2009.05.004>.

891 White, I., & Falkland, T. (2010), Management of freshwater lenses on small Pacific islands,  
892 *Hydrogeology Journal*, 18(1), 227-246. <https://doi.org/10.1007/s10040-009-0525-0>.

893 Yan, M., Lu, C., Werner, A. D., & Luo, J. (2021), Analytical, Experimental, and Numerical  
894 Investigation of Partially Penetrating Barriers for Expanding Island Freshwater Lenses, *Water*  
895 *Resources Research*, 57(3), e2020WR028386. <https://doi.org/10.1029/2020WR028386>.

896 Yang, J., Wang, Q., Heidbüchel, I., Xu, T., & Lu, C. (2025), Cut-off walls alter nitrogen loads and  
897 fluxes in small islands, *Journal of Hydrology*, 647, 132266.  
898 <https://doi.org/10.1016/j.jhydrol.2024.132266>.

899 Yao, Y., Andrews, C., Zheng, Y., He, X., Babovic, V., & Zheng, C. (2019), Development of Fresh  
900 Groundwater Lens in Coastal Reclaimed Islands, *Journal of Hydrology*, 573, 365-375.  
901 <https://doi.org/10.1016/j.jhydrol.2019.03.062>.

902 Yuan, C., Hu, L., Ren, Z., Xu, X., Gui, X., Gong, X., Wu, R., Sima, J., & Cao, X. (2024), Marine  
903 Microplastics Enhance Release of Arsenic in Coastal Aquifer during Seawater Intrusion  
904 Process, *Journal of Hazardous Materials*, 475, 134804.  
905 <https://doi.org/10.1016/j.jhazmat.2024.134804>.

906 Zheng, T. (2014), Numerical Analysis of Modeling Concepts for Salt Precipitation and Porosity -  
907 Permeability Evolution during Brine Evaporation.

908 Zheng, T., Meng, Y., Meng, X., Gao, S., Zhang, L., Zhang, B., Liu, T., & Luo, J. (2025), Influence  
909 of time-space variability of rainfall infiltration recharge on fresh groundwater lens, *Physics of*  
910 *Fluids*, 37(3), 036623. <https://doi.org/10.1063/5.0253940>.

911